

Special Section:

Forum for Arctic Modeling and Observational Synthesis (FAMOS) 2: Beaufort Gyre Phenomenon

Key Points:

- Dense water cascading is explored on multidecadal time scales in a 3-D pan-Arctic model, presenting good agreement with observations
- The cross-shelf water exchanges caused by cascading are estimated as 1.3 Sv of volume flux, thus exceeding the Bering Strait inflow
- Upwelling of Atlantic waters onto the shelf, followed by subsequent cooling and mixing, trigger cascading on the West Chukchi Sea shelf

Supporting Information:

- Supporting Information S1
- Movie S1
- Movie S2
- Movie S3
- Movie S4

Correspondence to:

V. V. Ivanov,
vladimir.ivanov@aari.ru

Citation:

Luneva, M. V., Ivanov, V. V., Tuzov, F., Aksenov, Y., Harle, J. D., Kelly, S., & Holt, J. T. (2020). Hotspots of dense water cascading in the Arctic Ocean: Implications for the Pacific water pathways. *Journal of Geophysical Research: Oceans*, 125, e2020JC016044. <https://doi.org/10.1029/2020JC016044>

Received 11 MAR 2020





Accepted 10 SEP 2020

Accepted article online 17 SEP 2020

©2020. The Authors.

This is an open access article under the terms of the Creative Commons Attribution License, which permits use, distribution and reproduction in any medium, provided the original work is properly cited.

Hotspots of Dense Water Cascading in the Arctic Ocean: Implications for the Pacific Water Pathways

Maria V. Luneva¹ , Vladimir V. Ivanov^{2,3} , Fedor Tuzov² , Yevgeny Aksenov⁴ , James D. Harle⁴ , Stephen Kelly⁴ , and Jason T. Holt¹ 

¹National Oceanography Centre, Joseph Proudman Building, Liverpool, UK, ²Geography Department, Moscow State University, Moscow, Russia, ³Arctic and Antarctic Research Institute, St. Petersburg, Russia, ⁴National Oceanography Centre, Southampton, UK

Abstract We explore dense water cascading (DWC), a type of bottom-trapped gravity current, on multidecadal time scales using a pan-Arctic regional ocean-ice model. DWC is particularly important in the Arctic Ocean as the main mechanism of ventilation of interior waters when open ocean convection is blocked by strong density stratification. We identify the locations where the most intense DWC events occur and evaluate the associated cross-shelf mass, heat, and salt fluxes. We find that the modeled locations of cascading agree well with the sparse historical observations and that cascading is the dominant process responsible for cross-shelf exchange in the boundary layers. Simulated DWC fluxes of 1.3 Sv (1 Sv = 10⁶ m³/s) in the Central Arctic are comparable to Bering Strait inflow, with associated surface and benthic Ekman fluxes of 0.85 and 0.58 Sv. With ice decline, both surface Ekman flux and DWC fluxes are increasing at a rate of 0.023 and 0.0175 Sv/year, respectively. A detailed analysis of specific cascading sites around the Beaufort Gyre and adjacent regions shows that autumn upwelling of warm and saltier Atlantic waters on the shelf and subsequent cooling and mixing of uplifted waters trigger the cascading on the West Chukchi Sea shelf break. Lagrangian particle tracking of low salinity Pacific waters originating at the surface in the Bering Strait shows that these waters are modified by brine rejection and cooling, and through subsequent mixing become dense enough to reach depths of 160–200 m.

Plain Language Summary In this study we explore dense water cascading, a specific type of bottom-trapped gravity current. This current of very dense waters originates on the shelves, due to winter cooling and sea ice freezing, and slowly propagates downslope to deep waters. It is specifically important in the Arctic Ocean as the main mechanism of deep water mass formation and carbon storage. We use numerical model of the Arctic Ocean to predict preferable locations of the cascading, its intensity mass, and heat fluxes. Our results are in agreement with available very sparse observations. Our model predicts that with sea ice melting, cascading formation will accelerate.

1. Introduction

Gradual reduction in Arctic sea ice cover in the 1990–2000s in response to global warming probably acted as a trigger for the accelerated transition toward a seasonally ice-free Arctic Ocean (Kwok et al., 2009). Enhanced ocean-air energy exchange, driving vertical mixing in the ocean, is a fundamental consequence of increasing exposure of the sea surface to atmospheric forcing. Multiple examples indicating that this effect is already at work at the margins of the Arctic Ocean deep interior have recently been reported (Ivanov et al., 2016; Ivanov & Repina, 2019; Lind et al., 2018; Polyakov et al., 2017; Timmermans et al., 2018).

One of the crucial processes contributing to the upper ocean to abyssal exchange in the Arctic Ocean is shelf convection, also known as dense water cascading (DWC), a specific type of bottom-trapped gravity current (Shapiro et al., 2003). At high latitudes, the dense waters feeding DWC are formed on shallow shelves in the cold season due to heat loss to the atmosphere, resulting in freezing and subsequent brine injection into the water column. Preconditioning of DWC happens if the convection reaches the bottom, forming a well-mixed water mass denser than the waters downslope. In this case, dense water propagates mainly along-slope (due to Coriolis forcing) and downslope (due to bottom friction) as a bottom boundary current, mixing with the ambient waters en route. Descending DWC waters interact with bottom topographic features such as sills and canyons (Chapman & Gawarkiewicz, 1995; Kämpf, 2005), with large-scale currents (Aksenov

et al., 2011; Ivanov et al., 2015) and form meanders and eddies due to baroclinic instabilities (e.g., Tanaka & Akitomo, 2001). After reaching the deep basin floor or the neutral density level (where the density in the plume equals the density of the ambient waters), the DWC plume spreads as either a bottom layer (Ivanov et al., 2004) or intrudes in the adjoining water column as a lens shape with specific thermohaline characteristics (Koenig et al., 2018).

In the Arctic Ocean, DWC is particularly important because of the strong stratification in the upper water column, making the ocean essentially two layered (e.g., Proshutinsky & Johnson, 1997). Extremely strong density gradients between the fresh upper layer and the underlying waters inhibit open ocean convection from reaching deep water. This makes DWC the only process capable of deep ventilation of the interior Arctic basins. Specifically, in Arctic and sub-Arctic regions, cascades may replenish water in the halocline (Aagaard et al., 1981), in the intermediate warm and salty Atlantic layer (Ivanov & Golovin, 2007), and in the deep layer (Falina et al., 2012; Quadfasel et al., 1988). Indirect evidence exists that DWC may contribute to the replenishment of the bottom water mass in the Canada Basin, thus making it saltier and warmer than the bottom water in the Eurasian Basin (Rudels, 1986). However, no direct measurements supporting this concept have been reported. The geography of cascading around the Arctic Ocean, as revealed by historical hydrographic data in the twentieth century, is nonuniform. The highest density of DWC events ever captured by direct measurements was observed in the East-Atlantic sector of the Arctic Ocean (see Figure 1 and Ivanov et al., 2004). Several DWC sites were also observed at the North American continental slope (see Figure 1 and Ivanov et al., 2004). However, the broad shallow shelves between the Laptev Sea and the Bering Strait are not suitable for dense water formation due to the extreme freshening of surface waters by river runoff. Recent high-resolution observations by submarine gliders captured submesoscale lenses filled with relatively cold and fresh waters in the core of the West Spitsbergen Current, west of Svalbard (Koenig et al., 2018). These lenses are highly likely to contain shelf waters that had cascaded downslope and intruded into the West Spitsbergen current at their neutral density levels.

With the transition toward seasonal Arctic sea ice cover, the DWC spatial distribution is expected to change. While the Eurasian Arctic seas progressively evolve to a permanently ice-free and well-mixed Atlantic-dominated hydrographic regime (Lind et al., 2018; Polyakov et al., 2020), the North American Arctic shelf seas acquire more pronounced seasonal features, with extended ice-free areas in summer (Timmermans et al., 2018) while remaining fully ice covered in winter. This change theoretically creates favorable prerequisite conditions for stronger salinization of water on shelves after the onset of freezing and for enhanced polynya activity in winter in the regions historically predisposed to polynyas (Cavaliere & Martin, 1994; Winsor & Björk, 2000). Ivanov and Watanabe (2013) hypothesized an increased rate of cascading waters in the future and found support for this hypothesis in an idealized modeling study and a global model, comparing 1986–1987 (more ice) and 2006–2007 (less ice) conditions in the Laptev Sea (Ivanov et al., 2015).

Being a localized and sporadic process and occurring mostly under sea ice in winter, DWC is hard to observe. So far, only 27 locations around the Arctic Ocean have been identified where DWC events were confirmed at some times within the entire period of instrumental observations (see Figure 1). To the best of our knowledge, there are no well-justified estimates of the net DWC fluxes on a pan-Arctic scale, except a very approximate one by Shapiro et al. (2003). In this study we make a first attempt to fill this gap by using model-based estimates of DWC and comparing them with other cross-shelf mass and heat flux estimates and their trends.

This study is performed within the framework of the Forum for Arctic Ocean Modeling and Observational Synthesis (<https://famosarctic.com/teams/Cascading>) and aims to evaluate the ensemble mean cross-shelf volume, heat, and salt cascading fluxes, along with their uncertainties. An ensemble of global and Arctic models with different resolutions (from 2 to 13 km in the Arctic) and with different types of vertical coordinates presents contributions from two Nucleus for European Modeling of the Ocean framework for ocean climate, research and operational oceanography (NEMO) model configurations. In this study, we introduce and test methods of flux evaluations at observed locations of DWC and estimate the possible strength of the cascading compared with other components of cross-shelf flux. We perform the first flux evaluation using the NEMO-shelf model with $1/4^\circ$ spatial resolution, explicitly simulated tides, and well-resolved benthic layers (Luneva et al., 2015). We also use output from a global NEMO model with $1/12^\circ$ spatial resolution but without tides and coarser vertical resolution to track the spread of the Pacific waters in the Arctic Ocean (Kelly et al., 2018).

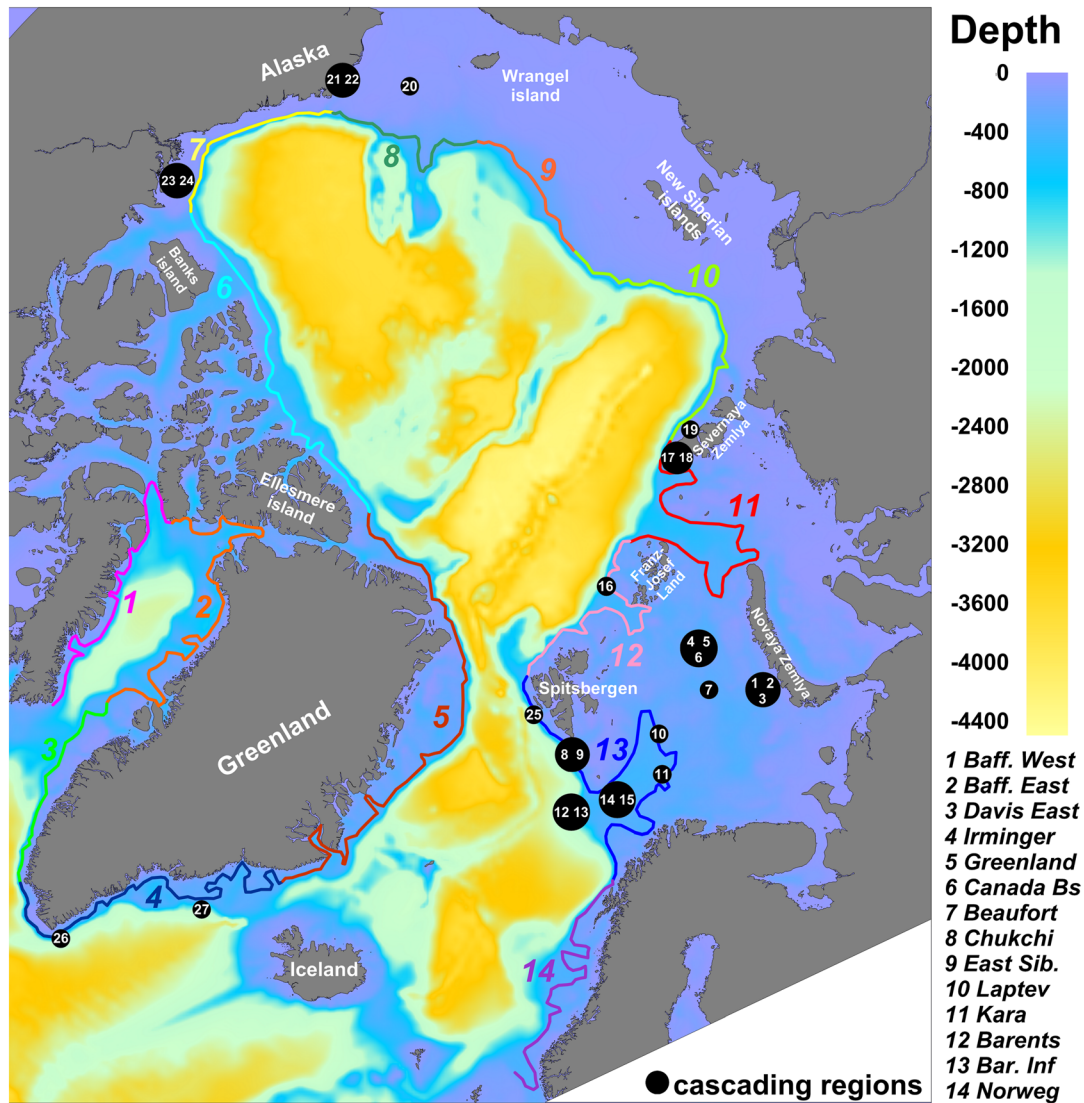


Figure 1. Locations of observed dense water cascading are shown in black circles. Numbers in each circle designate the observed cascading regions, as they are listed in Table 1. Contours of 300-m isobaths, used in analysis, are marked by color. The general bathymetry is defined by the associated color scale.

The paper is organized as follows. In section 3, we describe existing analytical estimates of DWC fluxes and methods to evaluate DWC and cross-shelf fluxes and discuss the importance of vertical and horizontal resolutions in simulations of DWC. Section 4 gives details on model setup and numerical experiments. In section 5, we present results for the entire Arctic Ocean, while section 6 focuses on case studies in the Beaufort and Chukchi Seas. Section 0 summarizes the findings and discusses the results in the context of the recent changes in Arctic sea ice.

2. Cascading and Cross-Shelf Fluxes Evaluation

2.1. Scaling and Theoretical Studies

The depth range to which dense water descends downslope depends on many factors. Horizontal density contrast across the shelf edge and the steepness of the slope are the major parameters that determine the speed of dense water propagation along the slope, the so-called Nof (1983) speed:

$$V_{\text{Nof}} = \frac{g s \delta\rho}{f\rho_o}, \quad (1)$$

where g is the gravity constant, $\delta\rho/\rho_o$ is the relative density anomaly in the dense plume compared with ambient waters, f is the Coriolis parameter, and $s = \nabla H$ is slope of bathymetry, H . The pace of cross-slope “spillage,” which is proportional to the Nof speed, together with density stratification in the ambient water, controls the ultimate depth of the dense plume spreading (Shapiro et al., 2003). In a laterally homogeneous 2-D case (with no variations along the shelf break), the dynamics of the downward-propagating dense front, in a steady state, are evaluated from a “1½-layer” model (Shapiro & Hill, 1997, their equation 22). That study incorporates bottom topography, Earth rotation, internal and bottom friction, and entrainment, as well as externally imposed pressure gradients, and defines the downslope-propagating velocity of a front as a fraction of Nof velocity which, for the case of a fully developed plume with maximal upstream thickness, is

$$V_{\text{down}} = 0.2V_{\text{Nof}}. \quad (2)$$

Following Ivanov et al. (2004), the observationally estimated Nof velocity is in the range of 2×10^{-3} to 0.35 m/s, which gives the downward (cross-slope) velocity 4×10^{-4} to 0.07 m/s. Theoretical estimate of the length scale of the thickness of a cascading plume is about $1.8h_{eb}$, where h_{eb} is bottom Ekman depth, which is defined for a flow with constant turbulent viscosity (A_v) as

$$h_{eb} = (2A_v/f)^{1/2}. \quad (3)$$

The resulting cascading flux is

$$F_{\text{casc}}^{\text{th}} = 0.36V_{\text{Nof}}h_{eb}. \quad (4)$$

Equation 4 is consistent with the laboratory experiments by Condie (1995) and Shapiro and Zatsepin (1997). Wobus et al. (2011), in a model with fine vertical resolution, reproduced the laboratory results. This suggests hydrostatic models are capable of reproducing the physics of cascading even on a steep slope, which is essential in the context of the current study.

On sufficiently steep slopes with large density gradients, the steady-state solution does not exist. Huthnance (2009) examined an initial value problem analytically and found that steady state exists when the dimensionless parameter

$$\beta = \frac{g|(s \cdot \nabla\rho)|}{f^2\rho_o} < 1. \quad (5)$$

If this condition is violated, the cascading flux accelerates with time and depth, and the thickness of the cascading tongue becomes much larger than the Ekman depth.

2.2. Processes Affecting Cascading

In the real ocean, cascading fluxes are affected by ambient stratification, ice conditions, along-slope geostrophic currents, and upwelling and downwelling caused by local and nonlocal winds and by eddies (Harden et al., 2014; Huthnance, 1995). If the cascading velocity is strong enough, Kelvin-Helmholtz instability will result in the entrainment of the ambient fluid, changing the density and thickness of the plume. At the edge of a plume, entrainment is likely in the benthic boundary layer. Mesoscale eddies may appear as a result of DWC flow instability and potential energy release, thus leading to increased cross-isobath water exchange (Platov & Golubeva, 2019).

Ivanov and Watanabe (2013) and Ivanov et al. (2015) suggested that a large seasonal variability of sea ice conditions on the shelves (ice-covered shelves in winter and ice-free in summer) would result in a stronger heat loss during ice-free period and brine rejection during new ice formation, thus leading to a stronger buoyancy loss and stronger cascading (Figure 2a). More extensive ice cover prevents heat loss and new ice formation, resulting in less dense water forming on the shelves. With the summer ice edge retreating

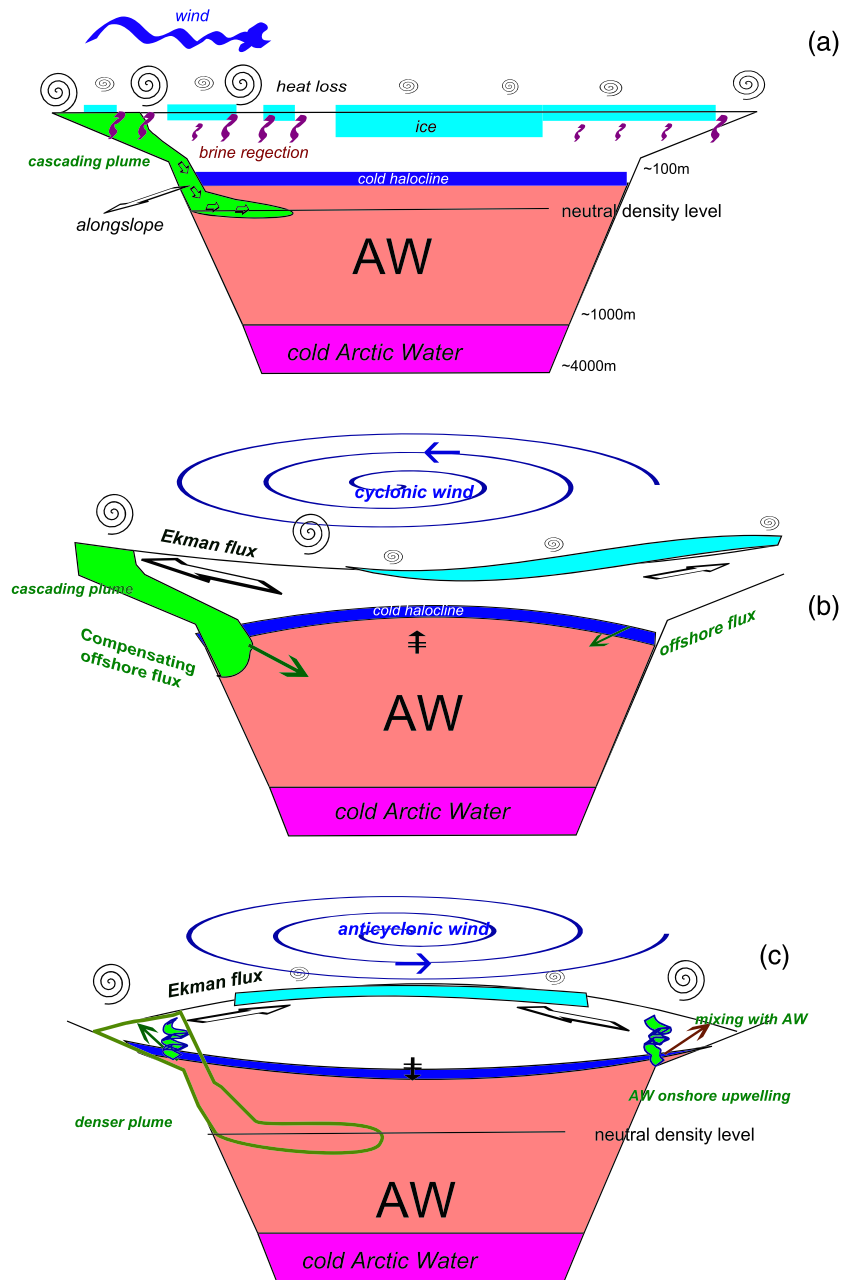


Figure 2. Schematics of the Arctic Ocean stratification, cascading process, and processes affecting cascading. Ice is indicated by cyan color, mixed upper waters remain uncolored, cold fresh halocline is shown by navy blue, pink is warm and salty Atlantic origin water (AW), magenta shows cold, salty Arctic abyssal waters, and green represents the cascading plume. (a) Ice concentration and offshore winds. Wind blowing offshore results in larger heat uptake from the ocean on the shelf, stronger ice formation, and brine rejection. A cascading plume (shown by green) forms on the shelf break, descends along the shelf break to the depth of ambient neutral density, and propagates along it. (b) Cyclonic winds move surface waters onshore, resulting in compensating downwelling, offshore fluxes in the benthic layer, and support descending cascading flux. (c) Anticyclonic winds produce offshore fluxes in the surface layers and compensating upwelling-onshore fluxes. This might result in uplift of warm and saltier AW, cooling, and ventilation of which would support the formation of the relatively dense waters in the plume and thus deeper cascading.

beyond the outer continental shelf and the pack ice transforming in the Marginal Ice Zone, due to break up by waves and wind over the shelf slopes (Aksenov et al., 2017), dense water forms closer to the shelf break. Offshore winds expose shelf waters to densification due to cooling and new ice formation, providing further preconditioning for cascading (Figure 2a).

In the Arctic Ocean, geostrophic currents closely follow the contours of f/H in a cyclonic manner, with the shelf to the right of the current (e.g., Aksenov et al., 2011). This causes a benthic Ekman drain of the shelf waters directed offshore, supporting downward water fluxes, while anticyclonic along-slope currents generate upslope Ekman flux (e.g., Bacon et al., 2014). In contrast, the effects of the wind and surface Ekman currents on DWC are not well understood. Basin-scale cyclonic winds drive water onshore in the surface Ekman layer, resulting in compensating downwelling in the benthic layer (Figure 2b). Therefore, cyclonic winds can enhance DWC. Basin-scale anticyclonic winds drive surface waters offshore, creating compensating upwelling in the benthic layer, thus impeding DWC (Figure 2b). Following this mechanism, we might expect a negative correlation between offshore surface Ekman flux (SEF) and DWC fluxes, although the details depend on the shelf topography that controls the pathways of compensating upwelling waters. On the other hand, anticyclonic winds in winter drive compensating flux of denser waters on the shelf (Proshutinsky & Johnson, 1997). This increases the ventilation and mixing of warm Atlantic waters with newly formed DWC water masses (Figure 2c). Cabbelling can also increase the density of the mixed waters. This effect can be compared with the preconditioning of deep convection in the Labrador Sea, where doming of isopycnals toward the surface supports ventilation and enhances deep convection (Marshall & Schott, 1999).

Wind-driven circulation can also change the freshwater pathways from the rivers along the Siberian and Canadian coasts (Timmermans et al., 2011), affecting stratification on the shelves. Local effects of winds may also force cascading waters across the shelf and off the shelf through the generation of Ekman downwelling cells (Harden et al., 2014). Examining DWC in the East Greenland shelf, the so-called Spill Jet Current, Pickart, Torres, and Fratantoni (2005) found that the combined effect of cyclonic barrier winds and eddies results in the strongest spilling events. The observed near-bottom intensified offshore currents exceeded 0.25 m/s, which is substantially more than the cross-stream velocities estimated from the steady-state theory of Shapiro and Hill (1997) and by Ivanov et al. (2004).

2.3. Flux Evaluation

To examine cascading, its preconditioning, and other components of cross-shelf exchange, we use model output (5-day means) for variables θ , S , u , v , w , $\vec{\tau}_s$, and $\vec{\tau}_b$ representing, respectively, potential temperature, salinity, velocity, and ocean shear stresses on the surface (ocean-atmosphere or ice-ocean). Bottom shear stress $\vec{\tau}_b$, if not present in the model outputs, is calculated as

$$\vec{\tau}_b = -C_D \vec{u}_b |\vec{u}_b|, \quad (6)$$

where \vec{u}_b is the velocity at the closest liquid grid point near the bottom and C_D is the quadratic bottom drag coefficient. Here we calculate the latter from the logarithmic law:

$$C_D = \max \left(\left(\frac{1}{\kappa \ln \left(\frac{\Delta z}{2z_0} \right)} \right)^2, 0.0025 \right),$$

where $\kappa = 0.4$ is the Von Karman constant, Δz is the near-bottom-layer thickness, and $z_0 = 0.001$ m is the bottom roughness. The tidal component of bottom stress is not considered in this formula, which could result in an underestimation of bottom shear stresses by 50% (Luneva et al., 2015).

All fluxes are calculated in the normal and along-slope directions and integrated over the particular depths relevant to each process considered. The modulus of the unit normal vector is

$$|\vec{n}| = |(n_x, n_y)| = |(\partial_x H, \partial_y H)| / \max \left((\partial_x H)^2 + (\partial_y H)^2 \right)^{\frac{1}{2}}, 10^{-10}. \quad (7a)$$

Then the normal and tangential components of velocity flux are

$$u_n = u n_x + v n_y, \quad (7b)$$

$$u_t = u n_y - v n_x. \quad (7c)$$

Here, u_n is taken as positive offshore, and u_l is positive while following contours of f/H , with shallow water on the right-hand side. We define ds_l as an element of the isobath and ds_n as an element of the contour directed downslope:

$$ds_n = \left((dx n_x)^2 + (dy n_y)^2 \right)^{\frac{1}{2}}, \quad (8a)$$

$$ds_l = \left((dy n_x)^2 + (dx n_y)^2 \right)^{\frac{1}{2}}. \quad (8b)$$

2.3.1. Preconditioning to Cascading

Here we describe conditions appropriate for the initiation of a cascading event. For water to be able to cascade downslope in the benthic layer, the mixed layer depth (*MLD*) on the shelf-slope must reach the bottom:

$$MLD(x, y, t) = H(x, y), \quad (9)$$

where *MLD* is defined by the density criteria, with threshold value of $\frac{\Delta\rho}{\rho_0} = 10^{-4}$, where $\Delta\rho$ is the density difference between the ocean surface and the bottom. If Condition 9 is satisfied, we define the mean salinity over the depth of mixed waters from sea surface ζ , to the bottom as

$$S_{ini}(x, y, t) = T^{-1} (H + \zeta)^{-1} \iint_{-H}^{\zeta} S \, dz \, dt', \quad (10a)$$

and density as

$$\rho_{ini}(x, y, t) = T^{-1} (H + \zeta)^{-1} \iint_{-H}^{\zeta} \rho \, dz \, dt'. \quad (10b)$$

Here, T is the period of temporal averaging (5 days in our case) over local variable $t' \in \left[t - \frac{T}{2}, t + \frac{T}{2} \right]$, and S is salinity. To separate well-mixed zones from the stratified areas, we set $S_{ini}(x, y, t) = 0$, $\rho_{ini}(x, y, t) = 0$ if 9 is not satisfied. The temperature of the mixed waters is typically at the local freezing point. If ρ_{ini} is larger than that of water downslope and the *MLD* reaches steep enough slopes, water will start to propagate along and downslope with the speed in the plume defined by the *Nof* velocity (if there are no other effects). We take a threshold value of the *Nof* velocity, defined by Equation 1, as $2 \times 10^{-3} \text{ m s}^{-1}$, consistent with observations (Ivanov et al., 2004). The condition for cascading then becomes

$$\begin{cases} u_n > 0; \\ \delta\rho \cdot s / \rho_0 < -2 \times 10^{-8}. \end{cases} \quad (11)$$

This is a weak condition because it corresponds to small density differences, only twice the threshold of mixed waters ($|\delta\rho/\rho_0| > 2 \times 10^{-4}$) and to weak slopes, $s = \nabla H > 10^{-4}$, corresponding to 1 m per typical $dx \sim 10 \text{ km}$ in our simulations.

We apply this condition to the adjacent model cells, where the density difference may not be large. The *Nof* velocity scale is relevant to the density difference across the cascading front, that is, between the maximum density inside the cascading plume and the density at the same depth in the undisturbed by cascading ambient water. The spatial scale of this front is expected to be much larger than the separation between adjacent model cells.

2.3.2. Offshore Cascading Fluxes

In practice, cascading fluxes are hard to separate from dense water flows of other origin. We identify a cascading flux as that where the denser water lies upslope and propagates downslope, subjected to condition 11. The cascading flux is then a mass flux, F_n^m , integrated over the layer $z \in (-H, -Z^*)$, that is, from the bottom to the upper plume boundary Z^* , where condition 11 is just satisfied.

$$F_n^m(x, y, t) = T^{-1} \iint_{-H}^{-Z^*} u_n \, dz \, dt. \quad (12a)$$

Corresponding salinity and heat fluxes are

$$F_n^S(x, y, t) = T^{-1} \iint_{-H}^{-Z^*} u_n (S - S_{\text{ref}}) dz dt, \quad (12b)$$

$$F_n^h(x, y, t) = T^{-1} \iint_{-H}^{-Z^*} u_n (\theta - \theta_{\text{ref}}) \rho c_p dz dt. \quad (12c)$$

Here, θ_{ref} and S_{ref} are reference potential temperature and salinity, and c_p is specific heat. F_n^m is always positive.

The choice of the reference values for the heat and freshwater fluxes calculations is not unique and depends on the focus of the analysis (e.g., see Bacon et al., 2015). For the purpose of this study, we use 5 years of mean benthic values to evaluate cascading fluxes with reference to the ambient waters. The relative salt flux anomaly (in freshwater volume flux units) is evaluated with reference to the 5-year mean salinity at the bottom, $S_{\text{ref}} = \bar{S}|_{z=-H}$:

$$F_n^S(x, y, t) = T^{-1} \iint_{-H}^{-Z^*} u_n \left\{ (S - \bar{S}|_{z=-H}) / \bar{S}|_{z=-H} \right\} dz dt. \quad (12d)$$

Finally, the height of the cascading plume is defined as

$$h_{\text{casc}}(x, y, t) = H - Z^*. \quad (13)$$

We also calculate theoretical estimate of the cascading flux, for conditions when all other forcing (along-slope currents, Ekman drains, and stratification of surrounding waters) are absent, given by Equation 3 (Shapiro & Hill, 1997).

As a theoretical estimate of DWC flux, we use Equation 3, V_{down} , defined by 2, and for a density contrast, $\delta\rho/\rho_0$, we take the maximal value in the dense water plume.

2.3.3. Ekman Surface and Benthic Fluxes

The theoretical estimates of the Ekman wind driven flux in steady state follow Gill (1968) and are independent of the choice of vertical eddy viscosity:

$$F_n^{\text{SEF}}(x, y, t) = -\tau_{sl}/(\rho f), \quad (14a)$$

$$F_n^{\text{BEF}}(x, y, t) = \frac{\tau_{bl}}{\rho f}, \quad (14b)$$

where $\tau_{sl} = \tau_{sx} n_y - \tau_{sy} n_x$ and $\tau_{bl} = \tau_{bx} n_y - \tau_{by} n_x$ are along-slope components of the surface and bottom shear stresses, applied to the ocean. Bottom shear stresses act in the opposite direction to the current, and steady-state Ekman flux is perpendicular to the shear stresses. In the Eurasian Arctic, where the near-bottom circulation is cyclonic (follows f/H contours; Aksenov et al., 2011; Gavilan Pascual-Ahuir et al., 2020), the bottom Ekman flux (BEF) is positive and offshore. If the wind circulation is anticyclonic, shear stresses applied to the ocean are negative, and the SEF is positive and offshore.

In a layer of constant viscosity A_v , a theoretical estimate of the surface Ekman depth, h_{es} , depends on the turbulent viscosity and the Coriolis parameter:

$$h_{es} = (2A_v/f)^{1/2}, \quad (15a)$$

and for a flow with constant shear, as often used in the atmospheric boundary layer (Wimbush & Munk, 1970):

$$h_{es}(x, y, t) = \kappa \left(\frac{\vec{\tau}_s}{\rho} \right)^{1/2} / f. \quad (15b)$$

Note that, unlike the Ekman fluxes ((14a) and (14b)), estimates of Ekman depths ((15a) and (15b)) are approximate and valid (and correspond to *MLD*) only in the unstratified case.

The benthic Ekman depth is an important parameter in this study. Indeed, the theoretically predicted thickness of a cascading plume is about twice the Ekman depth. Thus, the capability of the vertical discretization of the model to resolve the benthic Ekman depth at least in the initial stages of cascading is crucial in this study. Theoretical estimates of Ekman depth depend on the type of flow, presence/absence of tides (Prandle, 1982; Soulsby, 1983), and stratification. The commonly used Ekman depth boundary layer formulation, similar to the surface one 15b, was found to be typically smaller by a half than that observed in the ocean and shelf seas (Thorpe, 1988). Soulsby (1983) proposed (assuming $C_D = 1.9 \times 10^{-3}$)

$$h_{eb}(x, y, t) = \left(\frac{\tau_b}{\rho} \right)^{\frac{1}{2}} f^{-1}. \quad (15c)$$

In stratified conditions, Weatherley and Martin (1978) suggest

$$h_{eb}(x, y, t) = 1.3 \left(\frac{\tau_b}{\rho} \right)^{\frac{1}{2}} f^{-1} \left(1 + \frac{N}{f} \right)^{-1/4}. \quad (15d)$$

In our study we will use (15b) and (15c) for our estimates of surface and benthic boundary layers. Recalculating the expression with $C_D = 2.5 \times 10^{-3}$ gives

$$h_{eb}(x, y, t) \approx 0.043 |\vec{u}_b| f^{-1}, \quad (15e)$$

where $|\vec{u}_b|$ is the absolute value of velocity at the grid cell adjacent to the bottom, that is, twice as large as (15b) for this value of C_D . For typical near-bottom velocities (and Nof velocities; Ivanov et al., 2004) in the Central Arctic, we get $h_{eb} \approx 30$ m for a near-bottom velocity 0.1 m/s and $h_{eb} \approx 9$ m for a near-bottom speed 0.03 m/s.

In addition to the theoretical expressions ((14a) and (14b)), we estimate surface and bottom cross-shelf fluxes in the Ekman layers (thereafter SEFm and BEFm):

$$F_n^{SEFm}(x, y, t) = T^{-1} \iint_{-h_{es}}^{\zeta} u_n dz dt, \quad (16a)$$

$$F_n^{BEFm}(x, y, t) = T^{-1} \iint_{-H}^{-H+h_{eb}} u_n dz dt. \quad (16b)$$

Unlike the steady-state, balanced theoretical estimates of cross-shelf Ekman fluxes ((15a) and (15b)), SEFm and BEFm ((16a) and (16b)) also include cross-slope component of the geostrophic currents, for example, induced by mesoscale eddies, and contributions of cascading flux. Note that cascading depth and surface Ekman depths could be similar, especially at the preconditioning phase of cascading when all waters are well mixed from the surface to bottom: In this case we expect strong interactions of benthic-, surface-, and density-driven fluxes.

2.4. Effects of Vertical and Horizontal Resolutions

In the previous section we emphasized the importance of resolving the benthic boundary layers in the simulation of cascading. Horizontal resolution is another important issue, specifically related to the resolution of topographical features such as canyons and troughs, as these are preferred pathways for cascading plumes (Ivanov & Golovin, 2007; Kämpf, 2005). If the propagation speed of dense water is sufficiently high, eddies associated with baroclinic instability of the current and the interaction with eddies external to the plume may also play a role (Harden et al., 2014; Magaldi & Haine, 2015).

There are few studies examining the effects of resolution on the simulation of cascading. In idealized simulations of frictional downslope flow, Winton et al. (1998) found that a z -coordinate model gave results consistent with theory when the (1) horizontal resolution was high enough to resolve the slopes and (2) the vertical grid spacing resolved several points within the bottom frictional layer. Shapiro et al. (2013), on examining different vertical discretizations, found that their new hybrid scheme gave the best results both in

reproducing cascading compared with z coordinates and reducing pressure gradient errors compared with terrain-following s coordinates (Song & Haidvogel, 1994). This hybrid scheme, combined with the NEMO s -coordinates scheme, masking the very steep slopes (Madec & NEMO Team, 2016, Figure 4.5d), was applied only on the shelf, with z -partial steps elsewhere. A recent study by Bruciaferri et al. (2018) examines the effects of vertical resolution on an idealized numerical experiment of cascading in the Black Sea, imitating conditions of the Shapiro and Hill (1997) theory. Their model has a very fine horizontal resolution (~ 3.5 km, which is 7 points over a baroclinic Rossby radius of 20 km). However, they were unable to reproduce the analytical solution with z -partial steps vertical coordinates while successfully simulating it with hybrid coordinates on the shelf (the same type of coordinates as used by Shapiro et al., 2013, Luneva et al., 2015, and in current study). They found that using z coordinates resulted in spurious entrainment and a slowdown of the cascading plume by two orders of magnitude.

Several studies have examined similar issues of vertical coordinate type and resolution in the simulation of overflows (Colombo, 2018, 2020; Ezer & Mellor, 2004; Legg et al., 2009). Unlike cascading (see Table 1 from Legg et al., 2009), overflows are powerful flows with velocities ~ 0.5 – 1.5 m/s, large plume thickness (~ 100 – 300 m), and propagate long distances ($\sim 1,000$ km) across the ocean. Hence, unlike in cascades, nonlinearity (large Froude numbers), entrainment due to Kelvin-Helmholtz instability, and formation of eddies are crucial in overflow dynamics. In idealized overflow simulations, on constant slope, Ezer and Mellor (2004) examined the impact of both vertical and horizontal resolutions. They found that using terrain-following coordinates, locally or globally, significantly improves the representation of overflows: Eddies were reproduced in the model with a sigma-coordinate vertical grid and 10-km horizontal resolution (and low horizontal diffusivity), while in the z -level calculations, eddies develop only at a 2.5-km horizontal resolution. Increasing horizontal and vertical resolutions in the z -level grid converges the results toward those obtained by a much coarser horizontal resolution sigma-coordinate model. Similarly, a recent study by Colombo et al. (2020) found that using local terrain-following coordinates in the simulation of the Denmark Strait overflow with a $1/12^\circ$ model (~ 6 – 8 -km resolution) and 75 hybrid z - s -levels is equivalent to their best z -coordinate simulations with $1/60^\circ$ resolution (1–2 km) and 150 vertical levels. All the studies discussed demonstrate that refining the vertical resolution at some point compensates for coarseness of horizontal resolution.

3. Model Setup and Numerical Experiment

3.1. Pan-Arctic Model

In this study we use a medium-resolution (6–18 km) pan-Arctic regional NEMO model with explicitly resolved shelf processes (<http://www.nemo-ocean.eu/>). The horizontal resolution of the baseline model corresponds to a $1/4^\circ$ Ocean General Circulation Model (ORCA) global ocean model, but the vertical resolution is much finer across the shelf-slope, with terrain-following coordinates on the shelf, refining at the bottom to resolve the benthic layer. The model setup is similar to the regional pan-Arctic set up of Luneva et al. (2015, using NEMO v3.2) but featuring a number of improvements described below. A more-recent version of the NEMO model, v3.6 (Madec, 2008; O'Dea et al., 2017), is used in this study.

NEMO v3.6 has been modified and tested to include shelf sea and shelf-break processes (Luneva et al., 2015; O'Dea et al., 2017), explicitly simulating tides and resolving benthic layers with hybrid (terrain following-geopotential) vertical coordinates, and hereafter referred to as NEMO-shelf. To resolve tides, a nonlinear free-surface formulation with variable volume and mode-split explicit time stepping has been employed. However, it is noted that NEMO-shelf does not yet have the option for the low-diffusive, vertical piecewise parabolic advection scheme, which was available in NEMO v3.2 (used in Luneva et al., 2015).

The regional, pan-Arctic configuration considered here (see domain in Figure 3a) employs the mesh and topography from the global 0.25° NEMO tripolar grid (Madec, 2008) but reindexed to create a seamless rectangular model grid. Two open liquid boundaries are located in the Pacific Ocean (at 55°N) and in the Atlantic Ocean (near 48°N). The horizontal resolution corresponds to 18 km at the southern periphery of the domain, 12–13 km in the deep Arctic Ocean, 10 km on the Siberian shelf, and reduces to 6 km in the Canadian Arctic Archipelago. So, in these regions the horizontal resolution is comparable to models frequently used in shelf-ocean exchange studies (e.g., Holt et al., 2009). The model is eddy- and internal-tide permitting in the deep part of the Arctic Ocean but too coarse to resolve eddies and internal tides on the

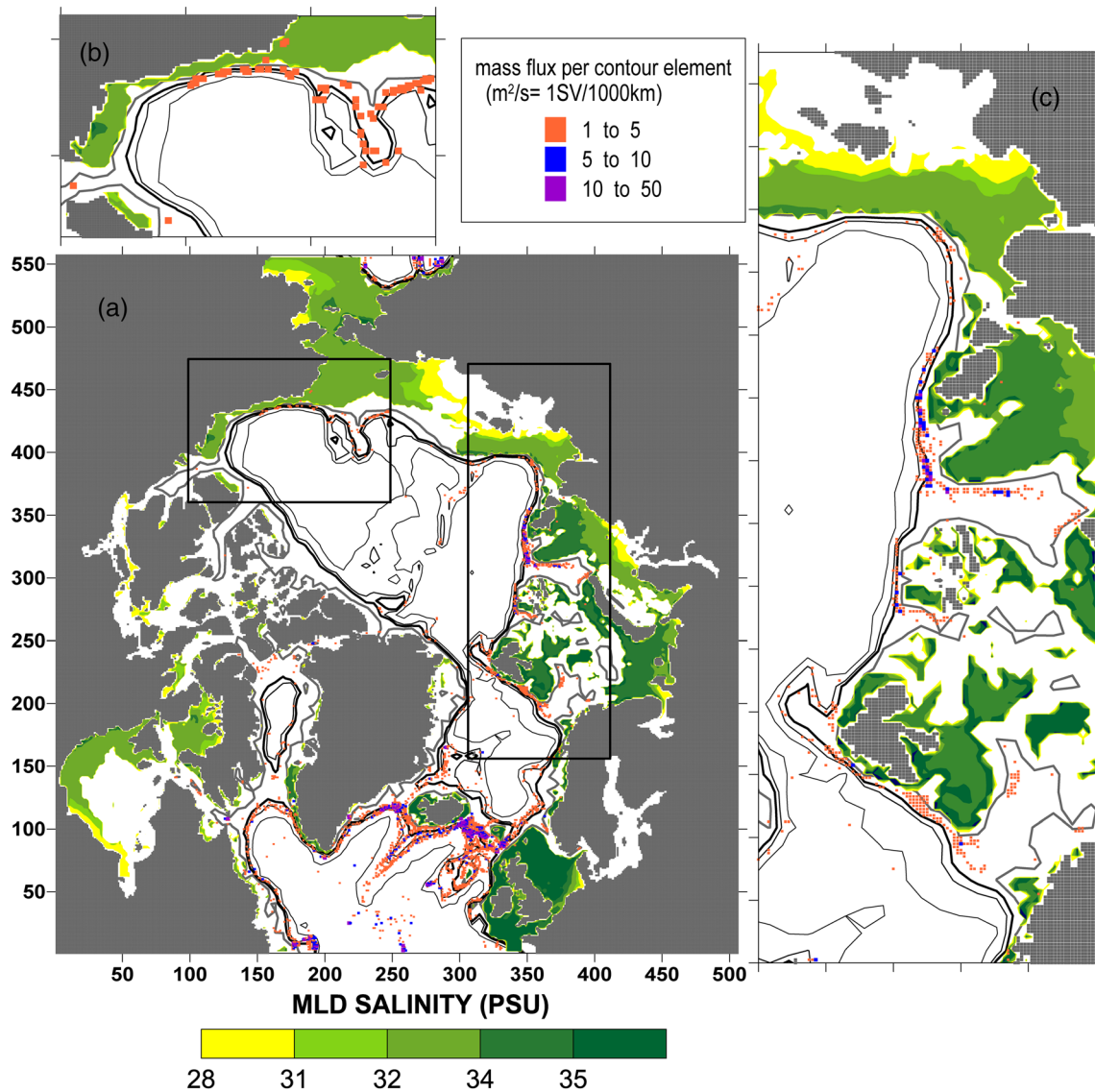


Figure 3. (a) Model domain, colored regions show preconditioning for cascading: maximum salinity of mixed waters over 25 years of simulations. Uncolored areas indicate that MLD does not reach bottom, so preconditioning is not satisfied. However, subsurface underwater cascading plumes are possible here. The 25-year mean DWC fluxes exceeding $1 m^2/s^2$ are shown by colored rectangles (see details in figure legend); (b, c) zoomed regions are denoted by rectangles in (a). Isobaths (1,000, 1,500, and 2,000 m) are shown by black contours and 300 m by gray contour.

shelf, where the first baroclinic radius Rossby is below 5 km. Vertical coordinates are prescribed by a generalized hybrid vertical coordinate (Shapiro et al., 2013), with finer resolution than that used by Luneva et al. (2015). The model has 74 vertical levels: 35 terrain-following s levels in the upper 300 m, condensing toward surface and bottom, and 40 partial-step z levels below. The s levels allow the resolution of the benthic boundary layer on the shelf with layer thicknesses near the bottom varying from 0.3 m in shallow water to 3 m at 300 m and naturally resolve the topographic slope (Winton et al., 1998). Vertical mixing/viscosity is defined by the $k-\epsilon$ closure with the Canuto et al. (2001) stability function. Lateral mixing is set by a Laplacian geopotential operator with the Smagorinsky (1963) parameterization. At the open ocean boundaries, lateral boundary conditions for the barotropic velocity and sea surface elevation are formulated with a flux-radiation scheme (Flather, 1976) and by a relaxation condition for tracers. The ocean model is coupled to the Louvain-la-Neuve Ice Model sea ice model LIM2 (Fichefet & Maqueda, 1997) with Elastic-Viscous-Plastic (EVP) sea ice rheology (Hunke & Dukowicz, 1997) adapted to the C-grid (Bouillon et al., 2009).

The initial and open boundary conditions for temperature, salinity, currents, and sea surface elevation and initial conditions for sea ice fraction and thicknesses are derived from 5-day mean fields from the global ORCA 1/12° NEMO integrations; see Aksenov et al. (2016) and section 3.2 for details. Our regional model is driven by geopotential tidal forcing with 15 constituents and lateral boundary conditions with nine tidal harmonics from TPX07.2, a 1/4° resolution inverse barotropic tidal model (Egbert & Erofeeva, 2002). Surface forcing is taken from DRAKKAR (2012) forcing set DFS5.1.1 reanalysis 3-hourly mean fields at 0.7° horizontal resolution. The forcing fields are interpolated on the model grid and used to calculate surface fluxes to the ocean and sea ice at each model time step following the CORE bulk formulae (Large & Yeager, 2004). The river runoff forcing data set is a combination of Greenland glacial freshwater runoff (Bamber et al., 2012) and Dai et al. (2009). The latter is interpolated on the model grids by the Total Runoff Integrating Pathways procedure (Oki & Sud, 1998).

The numerical simulations begin on 15 September 1979 with the model being spun up for the first 6 years. The analysis is performed for the following 25 years of the simulations, 1986–2010. No assimilation or restoring is used in the model.

3.2. Particle Tracking With Global High-Resolution Model

The global high-resolution eddy-permitting/resolving 1/12° ocean model (horizontal resolution of ~3 km in the Arctic Ocean and ~8 km globally) is used to drive Lagrangian particles, tracking the propagation of the Bering Strait waters and cascading in the Chukchi Sea (Kelly et al., 2018). The model is a z-level global ocean NEMO model (Madec & NEMO Team, 2016) coupled with the same version of the LIM2 ice model as the regional model described above. It simulates vertical mixing using the turbulent kinetic energy mixing scheme (e.g., Blanke & Delecluse, 1993). This global model does not include tides and, with full-depth z-partial steps, does not resolve the benthic boundary layers and shelf slopes as accurately as the regional model: At 100-m depth, the global model vertical grid is about 10 m and, at 300-m depth, is about 30 m.

For this Lagrangian analysis we use the Ariane numerical particle tracking tool developed at the Laboratoire de Physique des Océans in Brest, France (Blanke & Raynaud, 1997). The method calculates particle positions on the faces of the grid cells and solves the volume continuity equation on a C-grid, preserving local three-dimensional nondivergent flow: It is, therefore, capable of accurate volume tracing. The Ariane tool has been extensively used and validated for the Arctic (e.g., Popova et al., 2013) and globally (e.g., Van Sebille et al., 2018).

Model particles are released during the summer of 2001 (Kelly et al., 2018), with 100 particles initially seeded at the ocean surface over a regular 10 × 10 km grid in the Bering Strait. Releases take place every 10 days between the start of June and end of October (a total of 15 releases) to give a total of 1,500 trajectories. All particles are tracked for a full year and allowed to be advected horizontally and vertically, with particle positions recorded daily. The experiment design is the same as that used by Kelly et al. (2018). While having the advantage of being computationally fast with a good level of numerical accuracy in representing pathways of the water masses, the off-line particle tracking methods nevertheless do not include vertical mixing (see, e.g., Kelly et al., 2020, for further discussion and references). However, using the full 3-D velocity field allows us to track details of the mean vertical motion, which are key for the present study. Here we use the eddy-permitting/admitting model with ~3- to 4-km resolution in the area of the analysis, which accounts for the horizontal mixing primarily due to eddies. The Rossby radius in the area is ~5–10 km (Nurser & Bacon, 2014).

Both the global and regional model configurations are extensively validated in the Arctic against observations of hydrography, satellite dynamical topography and ocean circulation, and sea ice; see Luneva et al. (2015), Aksenov et al. (2016), Armitage et al. (2016), and Kelly et al. (2018, 2020) and Supporting Information S1.

In this paper we focus on results from the regional model with a comparatively coarse horizontal resolution but using high-resolution hybrid terrain following vertical coordinates on the shelf and explicitly resolved tides. Neither of these features are available in the 1/12° global model also used in this study. We expect that, particularly in the Central Arctic, cascading currents will be weak and plumes will be relatively thin in the vertical, and so the resolution of the benthic boundary layers is more important than capturing the eddying of cascading plumes.

Moreover, the horizontal resolution of the regional model corresponds to the $1/4^\circ$ ORCA global ocean model, which is currently used as a state-of-art ocean component for forecasting and climate coupled models (Storkey et al., 2018). Hence, analysis of this regional configuration is of particular interest, to examine the model skill in simulating DWC in a configuration relevant to future climate simulations in the Arctic and globally.

4. Results

We leave the detailed analysis of cascading fluxes in each of the Arctic domains to the intercomparison “cascading team” project and restrict this study to an overview. Figure 3 shows the maximum of “preconditioning” over 25 years, that is, the maximum salinity of well-mixed waters, defined by Equations 9, 10a, and 10b. These are the regions where cascading waters originate. Typically, these source areas are shallower than 200-m depth. Twenty-five-year mean dense water descending fluxes (only fluxes exceeding $1 \text{ m}^2/\text{s}$ are shown) are adjacent to these areas but do not necessarily directly fit the edge of the “preconditioning zone.” Note that the extensive spatial coverage of the dense water flux in Figure 3 does not mean that these events are repeated at the same place and the same year. Some of these expansive cascading locations could be the signature of the path of single or multiple cascading events. Animations (see supporting information for preconditioning and cascading flux) show intermittent sporadic events propagating along the slope and then descending when they reach steep slopes. These animations are consistent with the unsteady theory of Huthnance (2009), predicting the acceleration of cascading fluxes on reaching steep slopes.

In the North Atlantic, specifically near the western shelf break of the Labrador Sea, many events correspond to open ocean deep convection, reaching the bottom and then propagating as topographically trapped currents. Indeed, no preconditioning is seen in these locations. On the contrary, along the Greenland coast of the Labrador Sea and Irminger Sea (southwest slope of Greenland), preconditioning events are present along with intense cascading. Pickart, Torres, and Fratantoni (2005) and, later, Falina et al. (2012) identified signatures of multiyear spike-like cascading of fresher and colder waters down to 1,000–3,000 m in observations in the Irminger Sea. Our model simulations show the mean flux exceeding $10 \text{ m}^2/\text{s}$ in this location. Marson et al. (2017) performed detailed analysis of model-identified cascading events in the West Greenland Sea, including their preconditioning and pathways.

The strongest dense water fluxes appear in the North West Atlantic. These fluxes are related to cascading originating near the Iceland shelf break and to dense water overflows in the Denmark Strait and near the Faroe Bank Channel. In the Barents Sea, the model successfully simulates observed cascading events in the Barents Sea opening, around Svalbard (Spitsbergen) and Franz Josef Land. However, in the Barents Sea interior, shallower than 300 m, and near Novaya Zemlya, only two DWC locations are detected in the model, compared with 7 in the observations (Figure 1; actually only three locations, taking into account their proximity). On the west edge of the Spitsbergen shelf, the location with the strongest cascading flux corresponds well to the deep cascading detected by Koenig et al. (2018) (Location 25 in Figure 1 and in Table 1).

A preconditioning zone and intensive DWC locations are simulated on the shelf break of the Franz Josef Land Archipelago, corresponding to observed DWC in Location 16 (Figure 1 and Table 1).

The model predicts the intense dense water descending fluxes originating in St. Anna Trough, located in the Kara Sea (Figure 3b). These dense waters propagate cyclonically along the Severnaya Zemlya shelf break to the Laptev Sea, passing the East Severnaya Zemlya coastal polynya (Aksenov et al., 2010, 2011; Bareiss & Gørgen, 2005; Dmitrenko et al., 2009). Dense descending waters on this pathway have a mixed origin of shelf convection, overflows, and open convection in the polynya. In the southern and southeastern part of St. Anna Trough, simulated locations with the strongest flux are decoupled from the preconditioning area, showing that the origin of these fluxes are presumably overflows rather than DWCs. There are connections of preconditioning areas with strong descending fluxes in the northeastern part of St. Anna Trough and on the shelf break north of Severnaya Zemlya, suggesting that these fluxes refer to DWC events. Golovin (2005) observed DWCs in the latter region (west of the Laptev Sea shelf break; Locations 18 and 19 in Figure 1) and estimated the ventilation of intermediate waters due to cascading to be 0.06 Sv ($1 \text{ Sv} = 10^6 \text{ m}^3/\text{s}$). Ivanov and Golovin (2007) examined DWCs in this region using a fine-resolution numerical model and analysis of

Table 1
Coordinates and Locations of Observed DWCs (Figure 1) and Their Sources: Publication or Database

Region	No.	Reference
West Novaya Zemlya Shelf, Barents Sea	1	AARI archive and Ivanov et al. (2004)
West Novaya Zemlya Shelf, Barents Sea	2	Matishov et al. (1998) and Ivanov et al. (2004)
West Novaya Zemlya Shelf, Barents Sea	3	Matishov et al. (1998) and Ivanov et al. (2004)
West Novaya Zemlya Shelf, Barents Sea	4	Matishov et al. (1998) and Ivanov et al. (2004)
West Novaya Zemlya Shelf, Barents Sea	5	Matishov et al. (1998) and Ivanov et al. (2004)
West Novaya Zemlya Shelf, Barents Sea	6	Matishov et al. (1998) and Ivanov et al. (2004)
West Novaya Zemlya Shelf, Barents Sea	7	Matishov et al. (1998) and Ivanov et al. (2004)
Storfjord, Barents Sea	8	BarKode (1999) and Ivanov et al. (2004)
Storfjord, Barents Sea	9	BarKode (1999) and Ivanov et al. (2004)
Central Bank, Barents Sea	10	Quadfasel et al. (1992)
Central Bank, Barents Sea	11	Quadfasel et al. (1992)
Bear Island Channel, Barents Sea	12	BarKode (1999) and Ivanov et al. (2004)
Bear Island Channel, Barents Sea	13	BarKode (1999) and Ivanov et al. (2004)
Bear Island Channel, Barents Sea	14	BarKode (1999) and Ivanov et al. (2004)
Bear Island Channel, Barents Sea	15	BarKode (1999) and Ivanov et al. (2004)
Franz Victoria Channel, Barents Sea	16	BarKode (1999) and Ivanov et al. (2004)
St. Anna Trough, Kara Sea	17	BarKode (1999) and Ivanov et al. (2004)
St. Anna Trough, Kara Sea	18	BarKode (1999) and Ivanov et al. (2004)
Northeastern Severnaya Zemlya Shelf, Laptev Sea	19	AARI archive and Ivanov et al. (2004)
Eastern Chukchi Sea	20	WODA (1998) and Ivanov et al. (2004)
Barrow Canyon, Eastern Chukchi Sea	21	WODA (1998) and Ivanov et al. (2004)
Barrow Canyon, Eastern Chukchi Sea	22	WODA (1998) and Ivanov et al. (2004)
Beaufort Sea Shelf	23	Melling (1993)
Beaufort Sea Shelf	24	Melling and Moore (1995)
West Spitsbergen shelf	25	Koenig et al. (2018)
West Spitsbergen Shelf	26	Pickart, Weingartner, et al. (2005) and Falina et al. (2012)
East Greenland Shelf	27	Pickart, Torres, et al. (2005) and Harden et al. (2014)

observations and demonstrated the crucial role of the frequently occurring polynya in the area in the formation of dense water with potential for downslope descent to the warm core of the Atlantic origin waters at a depth of 300–400 m.

Our model captures cascading in a relatively shallow region of the Chukchi Sea with gentle slopes (21 and 22 in Figure 1) but fails to predict DWC near the mouth of the Mackenzie River (23 and 24 in Figure 1). However, the model does detect the preconditioning events there.

Substantial simulated DWCs coupled with preconditioning zones (Figure 3c) are located to the west of Mackenzie Bay, on the Beaufort Sea shelf. These locations lie on the pathway of Pacific Winter Water (PWW) propagating cyclonically from the Chukchi Sea as a boundary current (Zhong et al., 2018). As they deepen, these waters contribute to the deeper open sea anticyclonic PWW circulation and to the Beaufort Gyre (see schematics of currents in Zhong et al., 2018; Figure 12). The pathways of PWW, tracked in a finer horizontal resolution model by Lagrangian tracers, are discussed in more detail in section 5.4.

Thus, the model qualitatively predicts DWCs in the areas where cascading has been observed, shown in Figure 1. For quantitative estimates, we chose the 300-m isobath, since our model resolves the benthic boundary layer at depths shallower than this. The coarser z -partial step grid cells deeper than 300 m are unlikely to resolve the veering in the benthic Ekman layer and so not capture the correct balance of different physical factors in a cascading plume.

The along-slope distribution of cascading flux around the 300-m isobath (Figure 4a) is consistent with the spatial map in Figure 3. The strongest fluxes, reaching 3–4 m^2/s , occur on the Baffin Bay eastern slope, the Irminger Sea, and the Kara and the Barents Seas. Spatial and temporal variability is very strong, and the standard deviations exceed mean values in most places (Figure 4d). The SEFm is the dominant flux in the open-water regions, which are free of ice for most of the time (Figure 4b; note the difference in scale compared with Figure 4a). The DWC is the strongest component of cross-shelf exchange in the Arctic Ocean interior (sectors from 6 to 12 in Figure 1, thereafter the “Deep Arctic”). The standard deviation of SEFm is

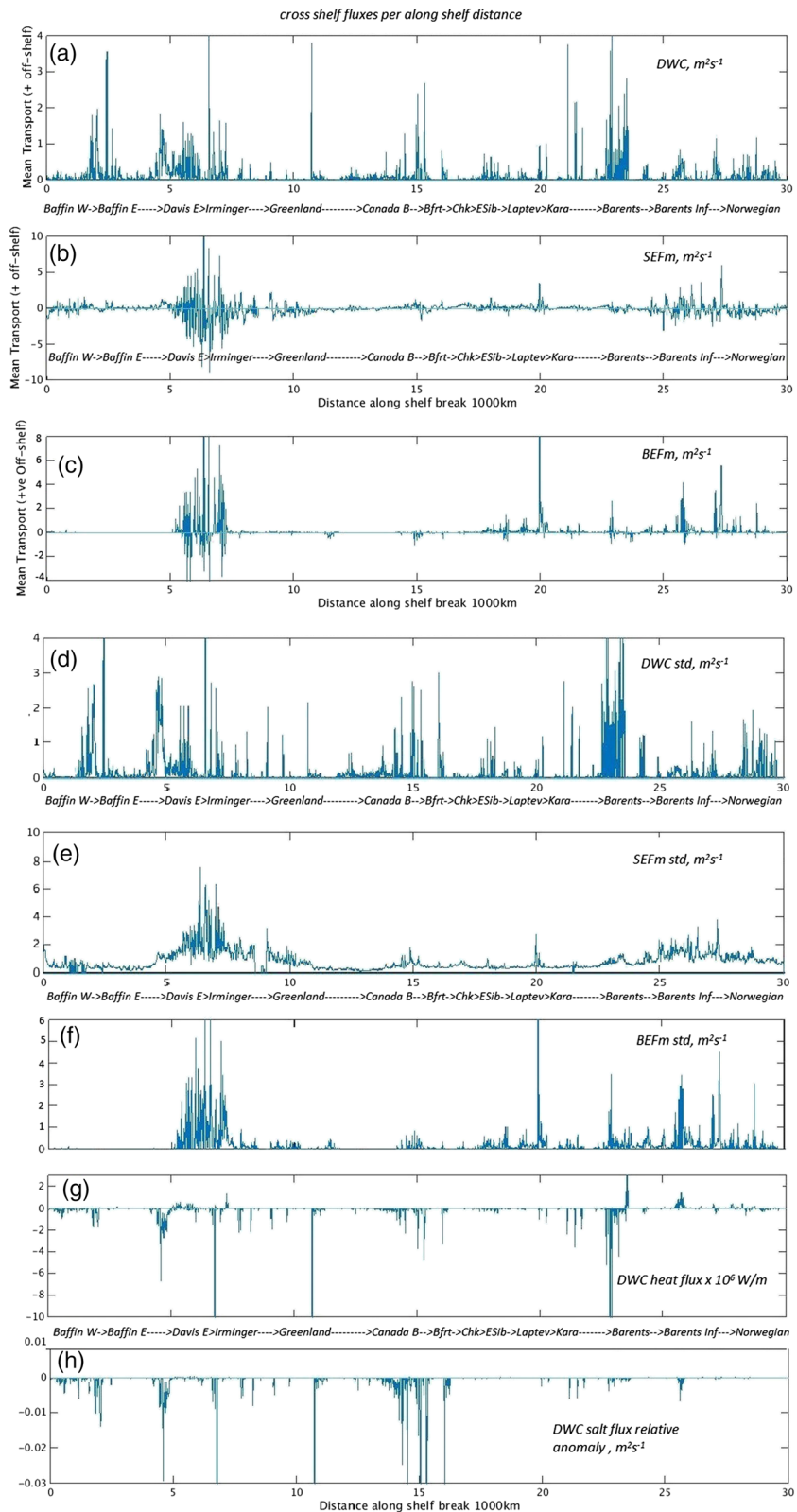


Figure 4. (a–c) Cross-isobath DWC, SEF, and BEF per length unit along the 300-m isobath around North Atlantic and Arctic Oceans. (d–f) Standard deviations of DWC, SEF, and BEF, (g) heat flux anomaly cascading flux relative to 5-year mean benthic temperature over the 300-m isobath, and (h) salinity anomaly flux, evaluated with 12d. Contoured sections are shown in Figure 1.

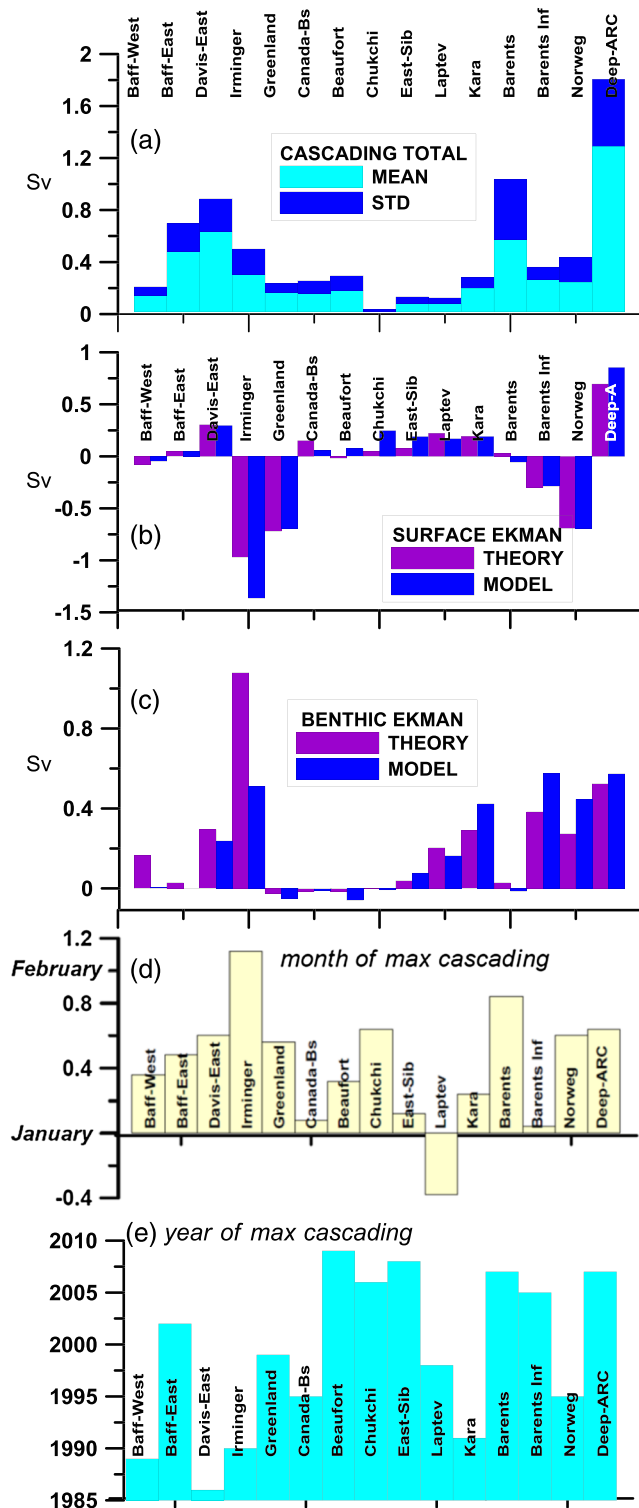


Figure 5. Properties of net fluxes, integrated over 300-m isobath sectors, shown in Figure 1. (a) Light blue 25-year mean DWC mass fluxes (Sv), and blue is standard deviations. (b) SEF 25-year mean (Sv), deep purple is evaluated from Equation 16a and blue from Equation 15a. (c) Same for BEF (Sv) but using Equations 16b and 15b. (d) Most frequent month of cascading maximum. (e) Year of maximal cascading flux.

approximately half the time mean values. The BEFm is highly variable in the open regions of the East Davis Strait shelf break and the Irminger Sea (Figures 4c and 4f). These values are small and negative in the Canada Basin and the Chukchi Sea due to the predominantly anticyclonic circulation and are mostly positive on the Eurasian shelf break (Aksenov et al., 2011). Small and negative BEFm are present also at the northern end of Greenland sector, corresponding to the anticyclonic branch in the Lincoln Sea, the pathway of the cold outflow from the Arctic Ocean to Baffin Bay through the Nares Strait. Small, negative BEFs also appear in the Barents Sea section, which could be linked to the inflow of Barents Sea Water to the deep Arctic Ocean through the Franz Josef Victoria Trough (or Victoria Channel), located between Svalbard and Franz Josef Land (40–45°E, 80–82°N). See Gammelsrød et al. (2009) and Aksenov et al. (2010) for the Franz Josef Victoria Trough location and a discussion of the ocean circulation in it. Standard deviations of BEFs are of the same order as or exceed the mean values (Figure 4f).

All DWCs in the Deep Arctic and the North Atlantic are temperature driven, with pronounced negative heat fluxes (Figure 4g). Salinity anomaly fluxes, given by Equation 12d relative to 5-year average bottom salinity on the 300-m contour, are small and negative (Figure 4h), indicating modeled DWC flux causes freshening in the bottom layer. This is consistent with observations in the Irminger Sea (Falina et al., 2012; Pickart, Torres, et al. 2005). Strong freshwater flux is simulated in the Canadian Basin, in the Beaufort Gyre, but is negligible in the Eurasian Basin. Negative heat flux and salt flux anomalies mimic each other along the 300-m isobath from the west side of Baffin Bay to the Beaufort Sea and are very small in the Eurasian sector.

In the Barents Sea inflow, there are small positive heat flux anomalies and small negative freshwater flux anomalies (i.e., implying a buoyancy flux of the wrong sign, assuming that cascading waters are denser). We attribute this to uncertainties in the definition of the reference temperature/salinity over the contour. Specifically, salinity and temperature in the DWC plumes vary with distance from the bottom, and the thickness of the plume varies in time and space. We take here the 5-year average bottom salinity/temperature as reference values. Mean salinity over the thickness of the DWC plume could be smaller, resulting in errors in the definitions of DWC heat and salt fluxes in regions with high temporal variability of water mass properties, such as the Barents Sea inflow.

Integrated over each sector (14 sectors are shown in Figure 1, and the 15th sector, the Deep Arctic, is the sum of 6–12), time-dependent Ekman fluxes correlated with theoretical values of SEF (BEF), given by ((16a) and (16b)) and model estimates of the Ekman depths ((15a) and (15b)) SEFm (BEFm) with correlations above 0.95 for SEFs and 0.74–0.97 for BEFs, except for Baffin East slope.

The 25-year mean cascading flux, following our estimates, is the dominant flux of cross-shelf exchange in the Arctic Ocean, reaching 1.3 Sv in the Deep Arctic (Figure 5a) and a maximal annual mean of 1.6 Sv. For SEF, the 25-year mean flux in the Deep Arctic is 0.85 Sv (65% of DWC; Figure 5b) versus 0.58 Sv of benthic drain (58% of DWC; Figure 5c).

Theoretical estimates of cascading flux, based on Equation 3 and constrained by conditions in Equation 11, exceed the direct model estimates by a factor of 10–30. This is not surprising considering the idealized

conditions used to derive the theory (Shapiro & Hill, 1997) based on laboratory experiments (Shapiro & Zatsepin, 1997) and idealized model experiments (Wobus et al., 2011, 2013) that consider the constant inflow of dense water on a cone with constant slope. Moreover, the estimate of downslope velocity in Equation 2 is valid for a steady propagating front. In the real ocean, the sporadic and unsteady blobs of dense water, formed during cold outbreaks over relatively short periods of time (2–3 months), propagate over irregular slopes under the influence of Ekman fluxes and geostrophic currents and eddies. The rate of dense water production depends on the conditions on the broad shallow slopes, where the Nof velocity is much smaller.

In the Deep Arctic, SEFs are reduced compared with less ice-covered areas, due to reduced atmospheric exposure. Positive offshore flux is a signature of anticyclonic winds (Figure 5b). The good agreement between magnitudes of simulated flux in the surface Ekman layer and theoretical estimates (SEF and SEF_m) and very high correlations show that the expression in Equation 15c for Ekman layer depth in the upper ocean is reasonably applicable and the geostrophic component of currents mostly follows bathymetry contours.

The most frequent month of cascading events over the 300-m isobath (Figure 5d) is calculated as follows: Each winter, from September to May, we define the month when cascading reaches a maximum for each sector and then average this maximum cascading flux over all years. The preferred month of cascading varies with region from late December to early February (Figure 5d). In general, more frequent cascading occurs from middle to late January. The year of maximal cascading shifts toward 2000–2007 in the Deep Arctic (Figure 5e). This period is characterized by a long-lasting period when anticyclonic atmospheric circulation dominates (Proshutinsky et al., 2015).

The flux integrated over the entire deep Arctic Ocean has very strong synoptic, seasonal, and interannual variability (Figure 6), reaching maximum values of 7 Sv for SEF, 3.5 Sv for cascading, and 1.5 Sv for the BEF. After filtering high-frequency synoptic variability (using 85-day running averages, approximating seasonal means), both SEF (Figure 6a) and BEF (Figure 6b) theoretical and simulated fluxes are very close. The seasonal peaks in BEF precede the peaks in DWC flux (Figure 6b). However, this may be a signature of enhanced benthic currents in summer and DWC in winter. After filtering the seasonal component (365-day running average; Figure 6c), there is no correlation evident between BEF and DWC. However, it is still not clear whether dense water flows contribute to cyclonic benthic currents or whether a benthic drain enhances cascading. All the yearly fluxes are positive, which is not surprising considering that the sectors are not closed, both laterally and vertically (i.e., only the boundary layers are considered). Moreover, these vertical boundary layers intersect in wintertime as the water column becomes well mixed during preconditioning. Thus, the cascading layer can include both surface and bottom Ekman layers (Figure 4). SEF and BEF layers can also overlap under the conditions of strong winds.

DWC fluxes are relatively small up to 1990: With an 85-day running average, they are less than 1 Sv. After 1990, with the acceleration of summer ice melt, DWC fluxes grow to a local maximum of 2.5 Sv during 1990–1995. This is a period when the cyclonic phase of atmospheric circulation dominates (Proshutinsky et al., 2015). Positive correlations between the seasonal cycles in SEF and DWC are evident for the period 1990–1995. This is followed by a 5-year period of negative correlations. The interannual variability (Figure 6c) does not show any obvious correlations. Different factors, discussed in section 3 (such as ice conditions, river runoff pathways, deflection by wind-driven circulation, and upwelling/downwelling regimes) are, presumably, location dependent and play conflicting roles on the feedbacks between net SEF and cascading.

Finally, both SEF and DWC have positive trends with time of 0.023 and 0.0175 Sv/year, respectively. Both trends may be explained by the sea ice decline, which enhances the transfer of momentum to the water compared with ice covered conditions, and also by the increase of new ice production on shelves, thus enhancing shelf convection.

5. Cascading in the Canadian Basin

Calculated flux values give a general estimation of the scale of mass and heat exchange by different processes between the shallow shelves and deep ocean. Although such estimation is very useful for understanding the significance of DWC in shelf-basin exchange on the pan-Arctic scale, it does not say much about the specific cascading events contributing to this integral flux. In this section we scrutinize time records of model output

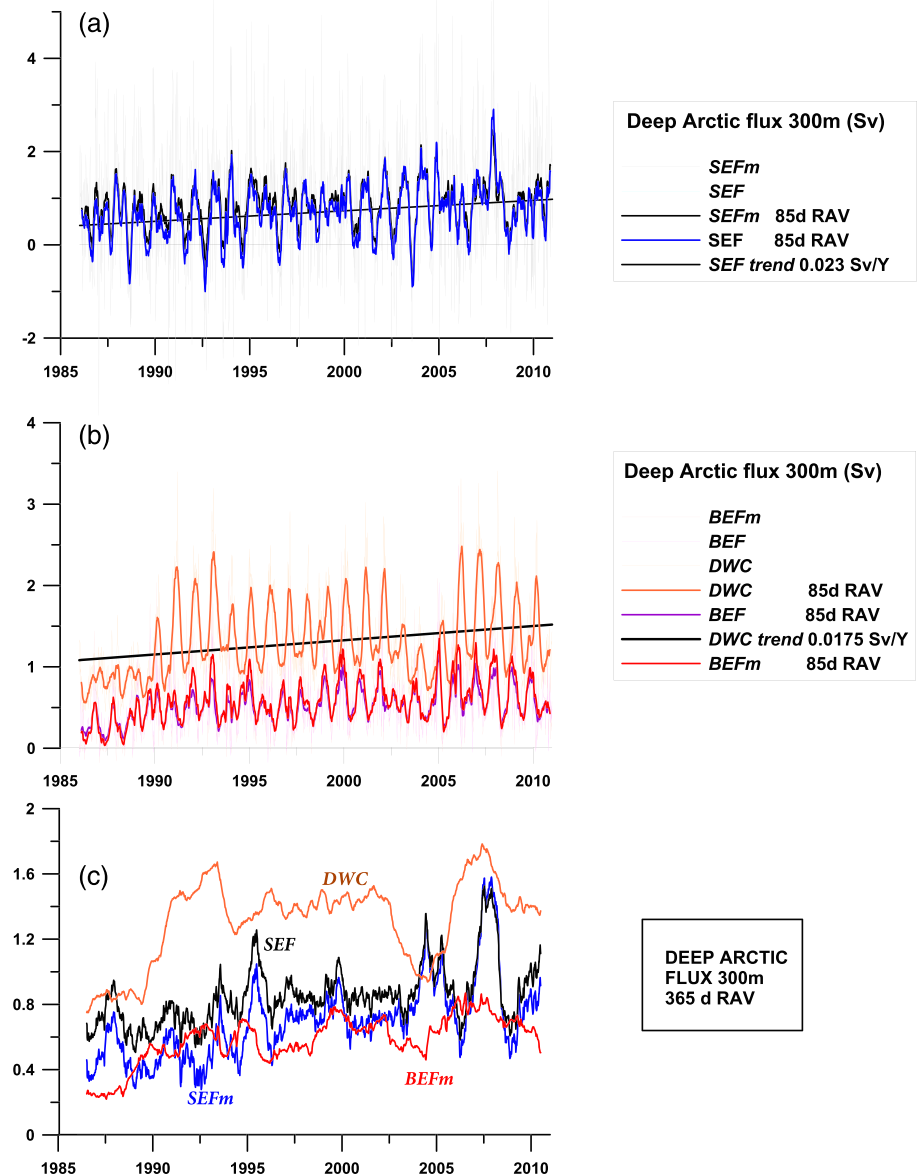


Figure 6. Time series of along-contour integrated fluxes across 300-m isobath in the Deep Arctic (Sectors 6–12 in Figure 1). (a) DW, SEF, SEFm, and their 85-day running averages. (b) DW, BEF, BEFm, and their 85-day running averages. (c) The 365-day running averages of DW, BEF, and SEF; colors are the same as in (b). Running averaging requires odd number of values, so a season corresponds to 17 consecutive 5-day mean values.

at several cross-slope sections around the Canada Basin shown in Figure 7, where cascading has been reported in historical data (Ivanov et al., 2004). A characteristic feature of the upper ocean layer at the margins of the Beaufort Gyre is the inflow of the Pacific-origin water, which enters through the Bering Strait. Thermohaline properties of the Pacific Water change seasonally between being warm and fresh in summer Pacific Summer Water (PSW) and cold and salty in winter Pacific Winter Water (PWW). At the entrance to the Canada Basin deep interior, the Pacific Water inflow splits into three branches: Barrow Canyon in the west (Pickart, Weingartner, et al., 2005), the Central Channel (Weingartner et al., 2005), and Herald Canyon in the east (Woodgate et al., 2005). As will be shown later, the distance of the area of interest from the Bering Strait plays an important role in the DW features and frequency. These case studies are now considered in some detail.

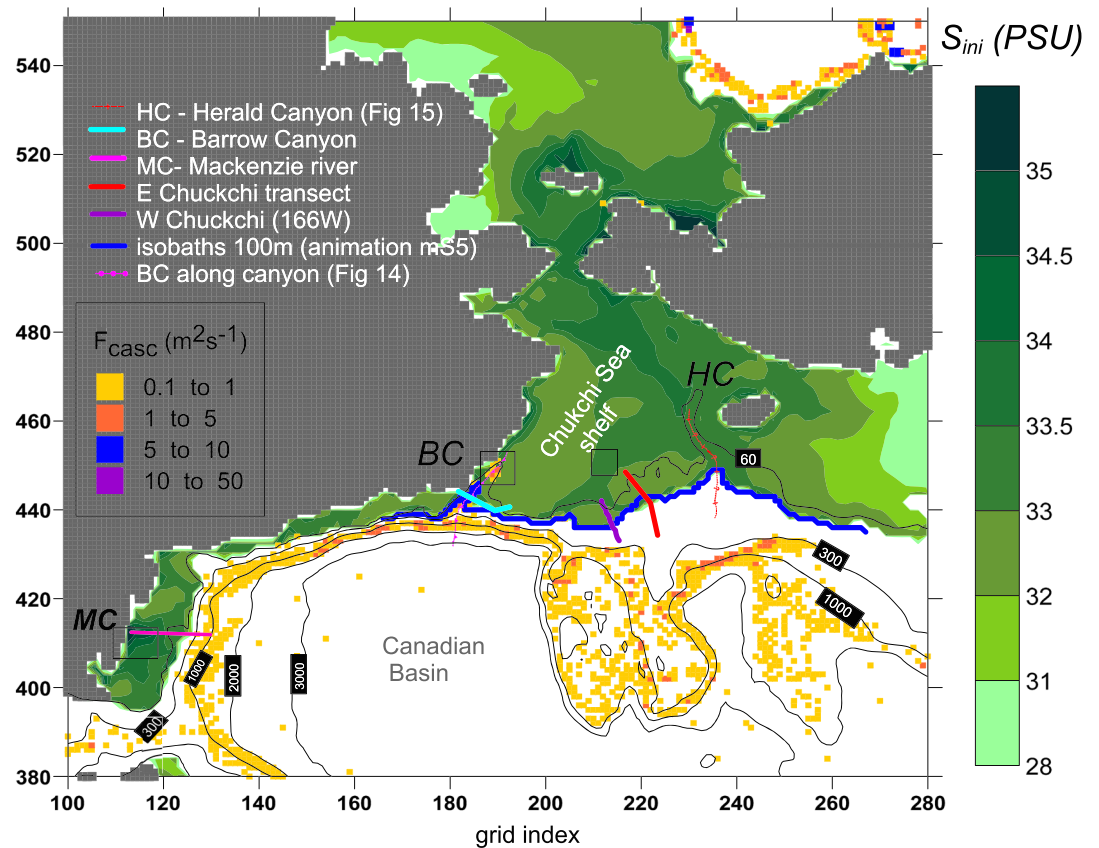


Figure 7. Zoom of Figure 1 in the Canadian Basin and the Chukchi Sea: location of the sections examined in section 6 and contour along isobaths 100 m used in Movie S3. S_{ini} (indicated by the green color) is the 25-year salinity maximum of waters mixed from the surface to the bottom. The locations of 25-year mean DWC fluxes are shown by the colored dots.

5.1. Beaufort Sea (Mackenzie River) Shelf

The shelf area off the Mackenzie River in the southeastern Beaufort Sea (Sector 7 in Figure 1, Locations 23 and 24) was reported by Ivanov et al. (2004) as the area where the fresh water over the shelf is occasionally substituted by relatively salty upwelling-origin waters. Freezing of this water leads to excessive salinization in the water column, causing surface-to-bottom convection and subsequent motion of the dense plume toward the shelf break. The broad and flat shelf (about 150 km to the steep slope) requires a substantial buoyancy deficit in the dense water to reach the shelf break without notable dispersion, in order to cascade down-slope. Direct measurements in winters 1981 and 1988 revealed large areas of surface water to the east of the Mackenzie mouth with salinity exceeding 33 Practical Salinity Units (PSU)—the value typical for 150-m depth in the adjacent deep basin. According to the assessment by Melling (1993), the mean volume transport of this cascade to the halocline layer in the long term is about 0.04 Sv.

The time-depth-distance plots (Figures 8a–8c) show the variations of the modeled near-bottom thermohaline properties for the entire model run. The characteristic feature of this section is two different regimes of the bottom water state. The threshold between these two regimes is in the middle of the record. Before 1998, the water on shelf is fresh and light almost all the time (except for 1988). Starting from 1998 until the end of the record, the frequency of winter events, when salty dense water occupies the entire shelf down to the shelf break between 66- and 164-m depth, substantially increases. The highest salinity/density on shelf, reaching those values in the adjacent basin at a depth between 164 and 362 m, is seen in winter 2008. Note that the winter 2008 followed the second successive summer minimum ice cover in the Arctic Ocean and particularly in the Canada Basin (Perovich et al., 2008). In winter 1988, the model data show a local extremum (on an interannual scale) of bottom salinity and density. This extremum coincides with

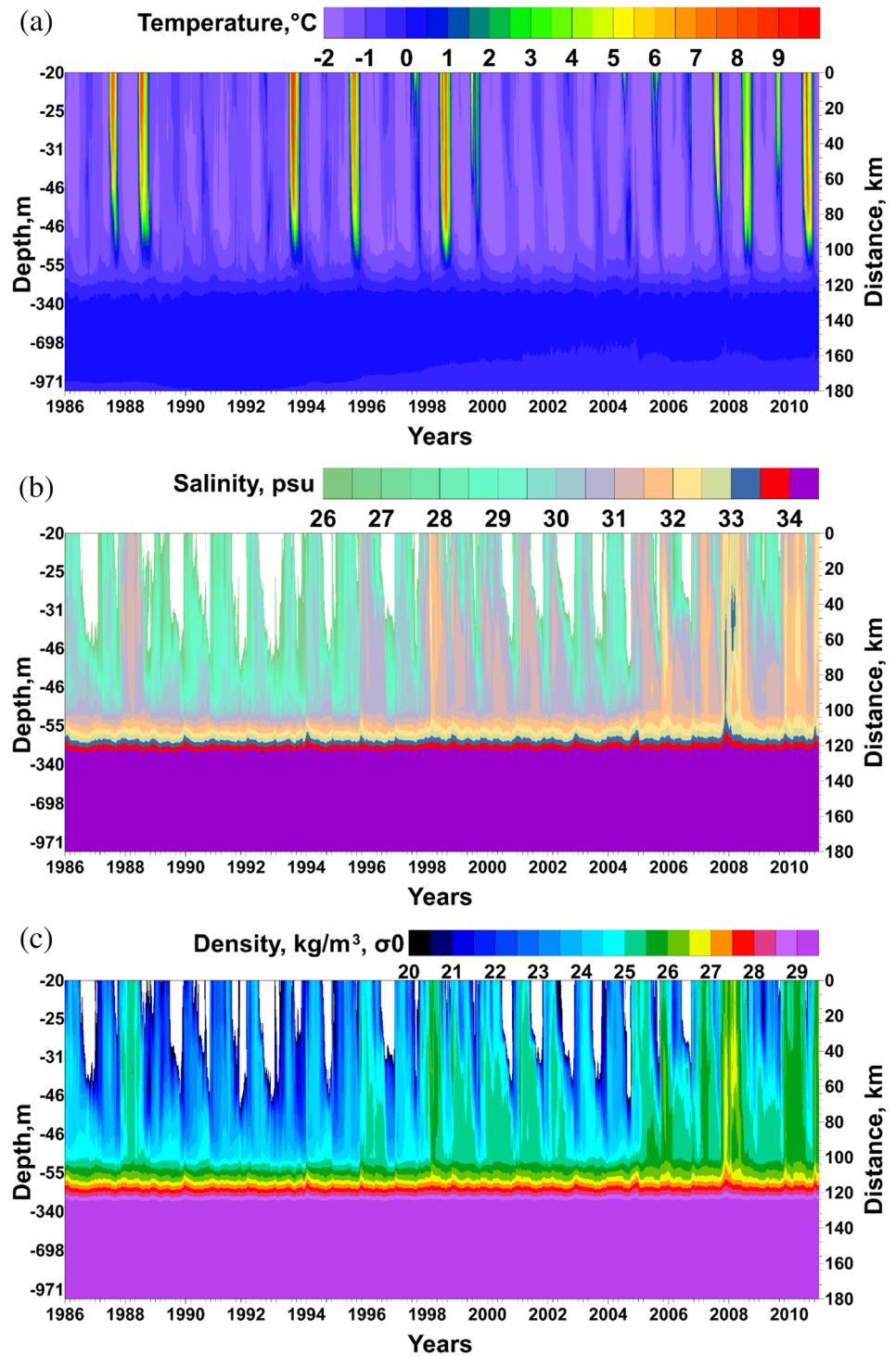


Figure 8. Time-distance plot of the modeled near-to-bottom thermohaline properties for the Beaufort Sea (Mackenzie) shelf-slope area: (a) temperature, °C; (b) salinity, PSU; and (c) potential density, kg/m³. The scale on the right the shows the distance along the sections (shown in Figure 7), and the scale on the left shows the corresponding depth of the sea along the sections.

the observed data, cited above. However, the modeled bottom salinity (about 31.5 PSU) is about 2 units less than that measured (over 33 PSU). On the other hand, the fact that the model correctly represents the case of favorable prerequisite conditions for cascading in winter 1988 implies that the tendency of generally increasing DWC potential in the 2000s is correctly captured by the model. The latter corroborates the general projection of intensification of cascading under conditions of increased seasonality of the Arctic sea ice cover (Ivanov & Watanabe, 2013).

5.2. Barrow Canyon

There is observational evidence of dense water downslope spilling at the southern flank of the Barrow Canyon (Cases 57 and 58 from Ivanov et al., 2004, here shown at Locations 21 and 22 in Figure 1 and Table 1). The relatively high density of this water mass permits the occasional penetration below the upper halocline in the Canadian Basin (Weingartner et al., 1998). Examples confirming this were reported in observations by Pickart, Weingartner, et al. (2005) and Hirano et al. (2016). DWC in the Barrow Canyon may be considered a rather rare event, at least in the past. For instance, even a dedicated survey in 1986–1987, specifically aimed at measuring the DWC down the canyon, failed to capture any signs of the process (Aagaard & Roach, 1990).

The time-depth plot of calculated near-to-bottom thermohaline properties for the entire model run is presented in Figures 9a–9c. Regular seasonal cycling of temperature and salinity in the water column is clearly visible down to the 80-m depth. Such regularity of a strong seasonal signal is not observed on the previously discussed Mackenzie River shelf (see Figure 8). The probable cause of this is the stronger impact of the alternating PWW and PSW, due to the proximity of the Barrow Canyon to the Bering Strait.

The shelf area between Cape Lisburne and Point Barrow along the Alaska coast, including Barrow Canyon, is the domain of the Barrow Coastal Polynya (Winsor & Björk, 2000). In winter, the ocean surface is rapidly cooled to the freezing point. Subsequent brine rejection and associated salinification of the water column inside the polynya provide the prerequisite conditions for DWC. However, as previously mentioned, the rare occurrence of cascading events in the past points to some concurrent processes blocking DWC development despite generally favorable background conditions. According to Hirano et al. (2016), a potential process is the upwelling of warm water forced by the persistent northeasterly winds. Hirano et al. (2016) argue that a rapid salinity drop after the termination of upwelling typically prevents preconditioning of shelf convection by the process suggested by Aagaard et al. (1981), thus explaining the rarity of cascading events in this region.

The time record of model salinity (Figures 9b and 9e) shows salinity exceeding 32.8 PSU over the shelf between 16 and 70 m during the winters of 2000, 2004, and 2007. In 2000 and 2004, the time intervals of extremal salinity did not exceed 7–10 days. In 2007, the residence time of extremely salty water on shelf was between mid-March and the end of June, thus pointing to a high probability of DWC. The vertical distribution of model potential density and salinity at the transect across the Barrow Canyon in February and April 2007 is shown in Figures 10a and 10b. The formation of a compact dense “pool” of water near the bottom and to the north of the canyon in February is probably the result of polynya formation. The model does not resolve the details of polynyas well; however, it shows repeatable appearance of ice concentrations below 0.9 (Figures 10c and 10d) at the edge of the coastline and near Barrow canyon in the period from January to April 2007. Polynya formation is further corroborated by the freezing point temperature and local salinity maximum from surface to bottom. By mid-April, the most salty and dense water accumulates along the center of the canyon, acquiring potential for further motion toward the mouth of the canyon as described by Pickart, Weingartner, et al. (2005).

5.3. Western Chukchi Sea

The vast and shallow shelf adjacent to the Bering Strait on the Arctic side is the pathway of the central branch of spreading Pacific-origin waters (Weingartner et al., 2005). Observational evidence of a cold dense water “pool” sitting on the outer shelf in this region is provided by Ivanov et al. (2004); see Case 20 in Figure 1 and in Table 1. The main difference in terms of dense water formation at this site, when compared to the previous two, is the very flat, extended, and shallow seabed. This fact explains why the preconditioning of DWC in this region substantially differs from those described above: They had initial replacement of

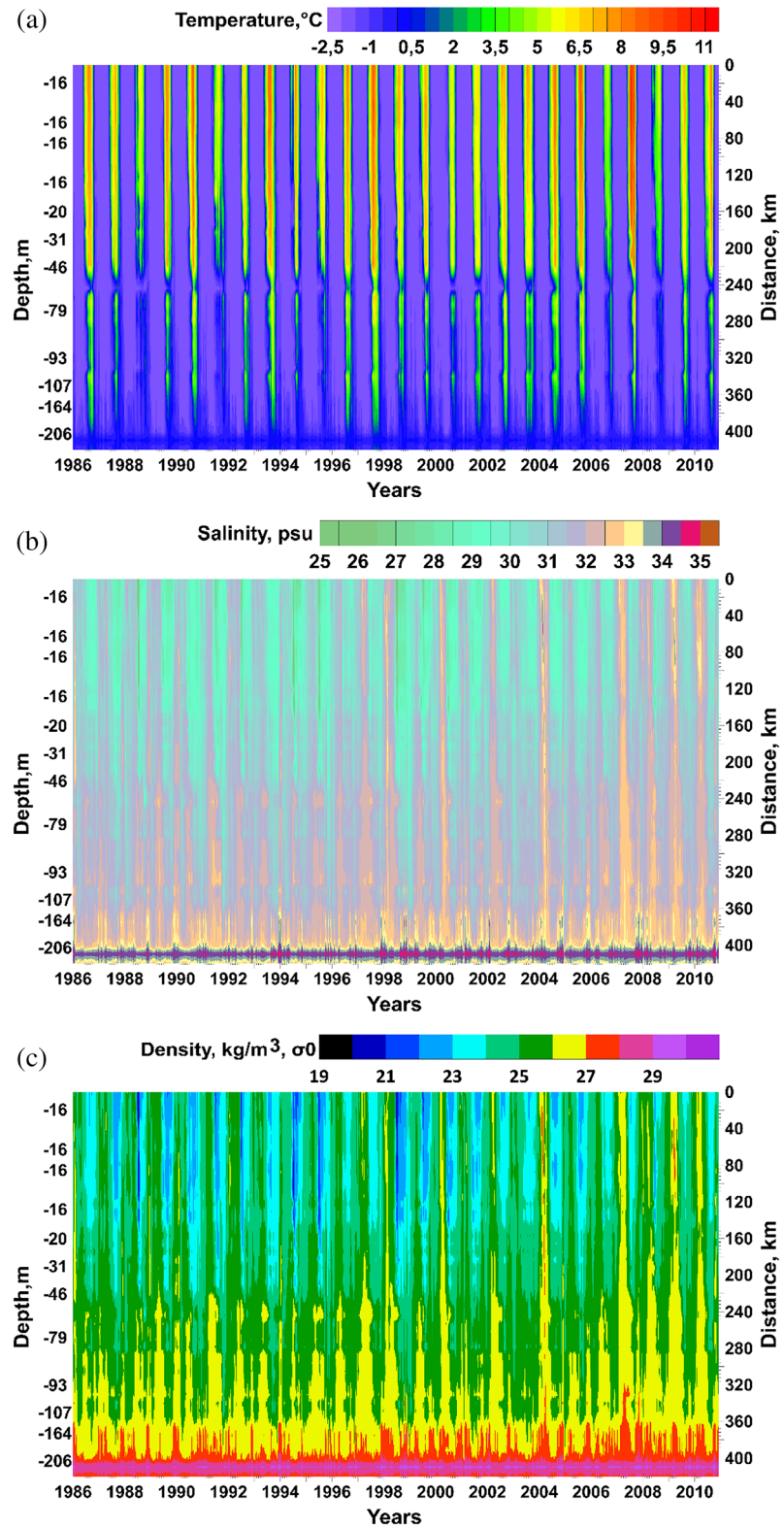


Figure 9a. Time-distance plot of the modeled near-to-bottom thermohaline properties for the Barrow Canyon, 1986–2010: (a) temperature, °C; (b) salinity, PSU; (c) potential density, kg/m³; (d–f) same as (a)–(c) but for the period 2000–2009.

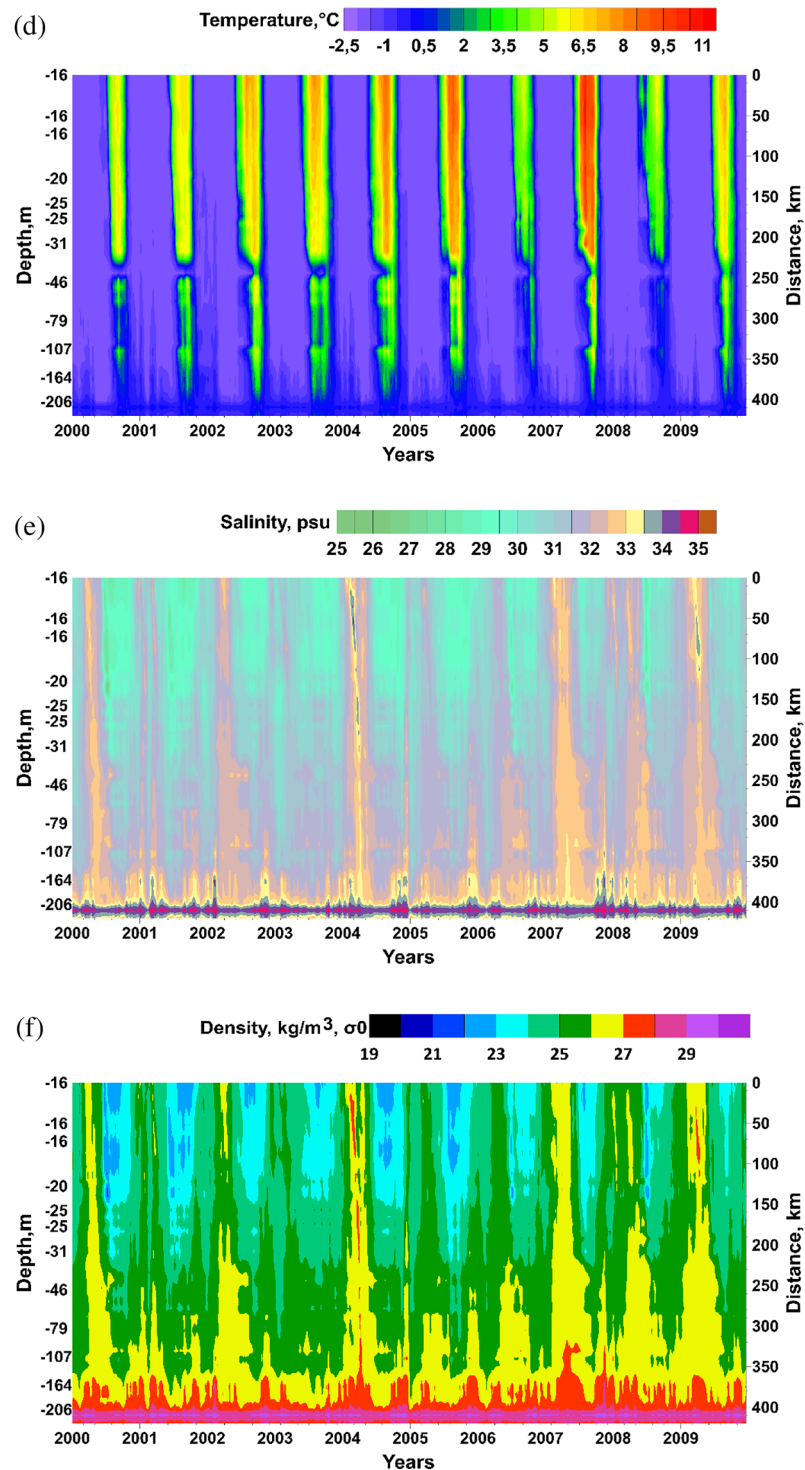


Figure 9b. (continued)

shallow fresh waters by salty upwelling-origin waters from the deep. For the Western Chukchi Sea, the major driving factor of dense water formation is the large extent of ice-free area in the autumn.

The characteristic feature of the modeled salinity/density time record, presented in Figures 11a–11c (cf. Figures 8 and 9), is the frequent occurrence of separate salty/dense periods in the upper shelf region (excluding the shelf break). This fact may be interpreted as the signature of localized surface-to-bottom

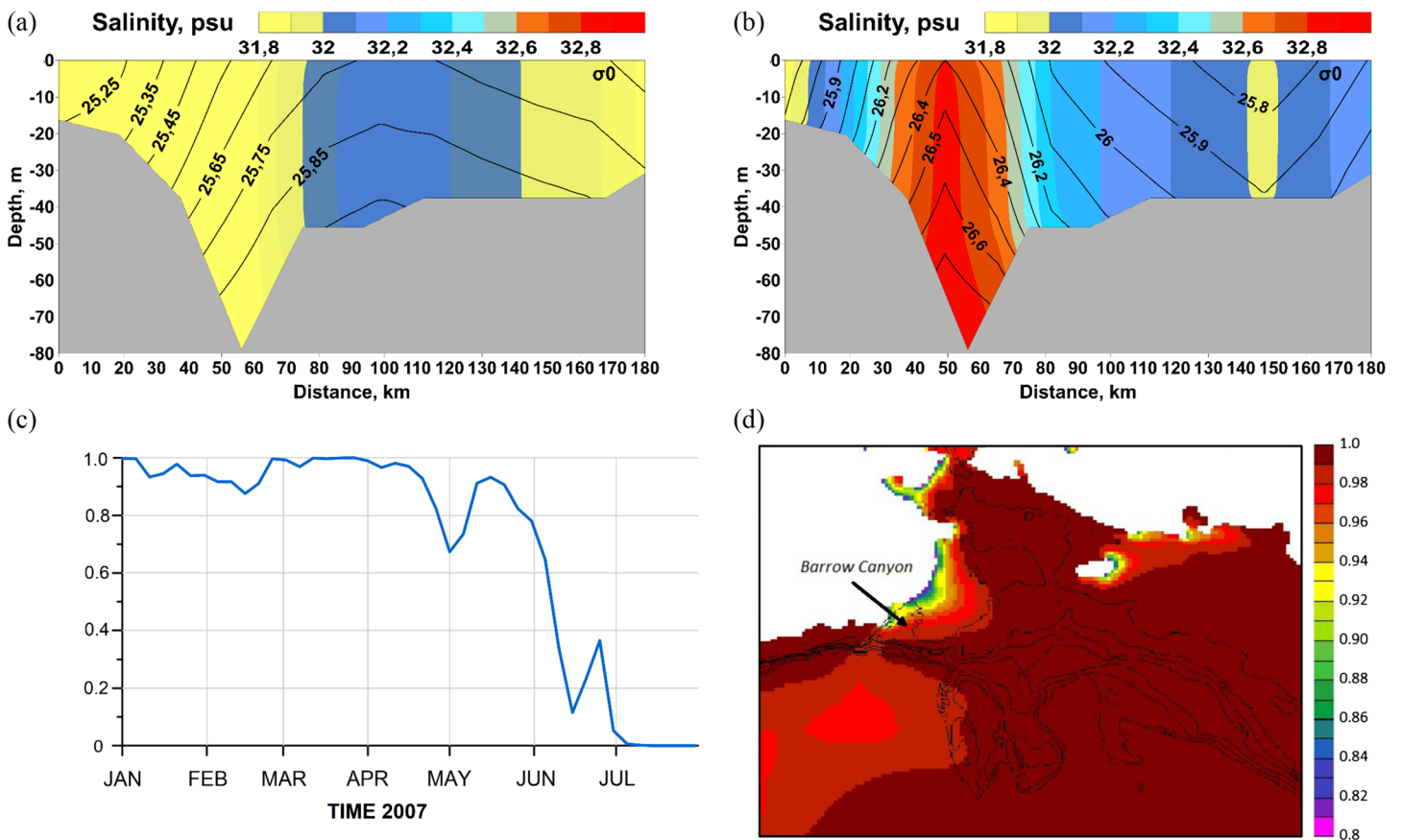


Figure 10. Vertical distribution of salinity (color shading) and potential density (contours) at the transect across the Barrow canyon (see Figure 7): (a) 5 February 2007; (b) 6 April 2007; (c) ice concentration averaged over the base of Barrow Canyon; and (d) ice concentration at 17 February 2007.

thermohaline convection, forming solitary dense water pockets that decay before reaching the shelf break. The reason behind this decay is the shallow slope and associated small Nof speed, implying that moving dense water patches have time to decay by horizontal and vertical mixing before they descend into the deep basin. However, there are three instances (1996, 1998, and 2008), when DWC into the deep basin down to a depth of 150–180 m can be anticipated on the basis of the model. The vertical transect of salinity and potential density across the shelf and the upper slope of the central Chukchi Sea is shown in Figure 11d. The pattern of density contours with maximum values on shelf near the bottom shows cascading of cold salty water from 60–80 to 100–120 m along the slope. The local maximum of salinity within the entire depth of the water column at 40–60 m indicates the source area of dense water formation, possibly linked with polynya formation.

Other evidence of DWC in this area was obtained by Conductivity-Temperature-Depth (CTD) measurements in July 2002 and in September 2004 (Pickart et al., 2009; Pickart, Weingartner, et al., 2005). Vertical transects of potential temperature and salinity, the latter roughly coinciding with the pattern of potential density for water near the freezing point, based on July 2002 data and on the model results for the same date, are presented in Figure 12. Both the observation and model results show a plume of cold and relatively fresh water that descends from the shallow shelf (~20–50 m) down to the deeper water (~100–120 m). Model simulations emphasize increased vertical mixing in the descending plume (Figures 12c and 12d), with diffusivity exceeding the background value by an order of magnitude. The plume meets the salty and warm Atlantic origin water at the intermediate depth. This warm and salty water sets the vertical limit for the descending plume, which then detaches from the seabed and spreads to the east along isobaths within the 80- to 120-m layer (Pickart, Weingartner, et al., 2005; Figure 12a). The modeled vertical bound of DWC spreading in this area is rather stable. The lower limit, as was captured by the model in March 2008 (see Figure 11d), is the same as was measured in summer 2002.

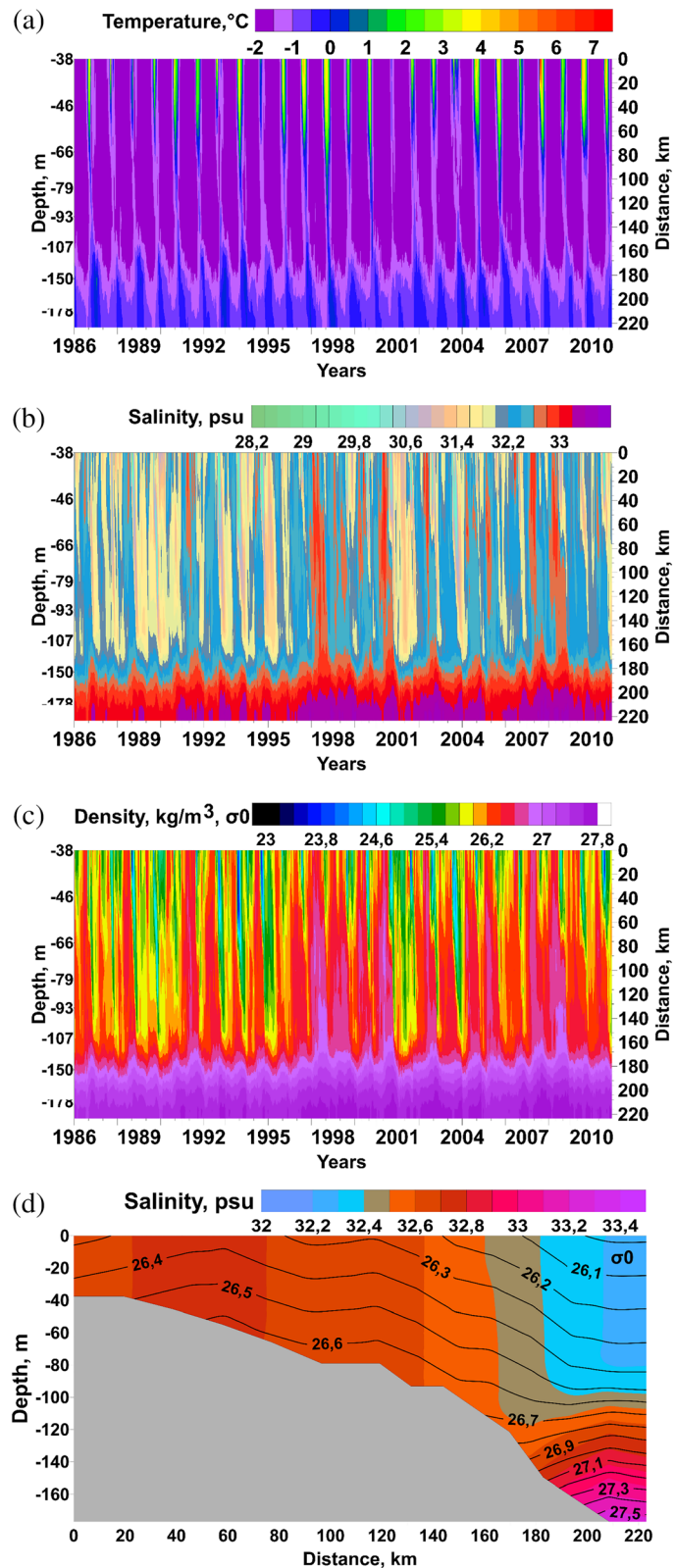


Figure 11. (a–c) Time–distance plot of the calculated near-to-bottom thermohaline properties for the Western Chukchi Sea shelf-slope area: (a) temperature, °C; (b) salinity, PSU; and (c) potential density, kg/m³. (d) Vertical distribution of salinity (color shading) and potential density (contours) at the transect across the Western Chukchi Sea shelf-slope area on 21 March 2008.

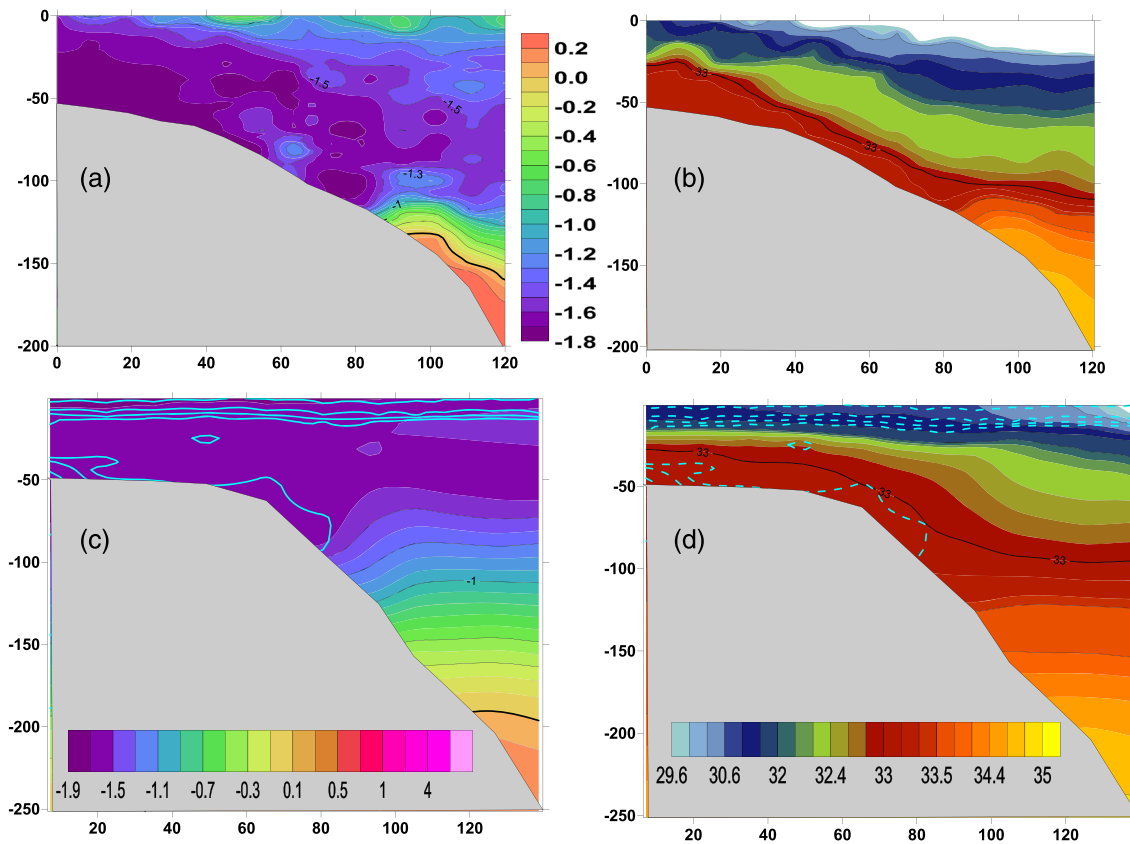


Figure 12. Vertical distribution of (a) temperature and (b) salinity along 166°W between 73°N and 74°N as measured on 19 July 2002 (Pickart et al., 2010; Pickart, Weingartner, et al., 2005) and (c, d) reproduced by the model. Model data are 5-day averages for 15–19 July 2002.

Animations of water properties—temperature, salinity, density, and vertical diffusivity along 165.5°W, located just one grid point apart from (Pickart et al., 2009) transect—are shown in Movie S3 and illustrate the subsequent stages of cascading process across the shelf: (i) uplifting of the warm salinity tongue (December 2001), (ii) formation of the blob of cold and saltier waters below the fresh and cold subsurface layer at ~73°N, and (iii) the ventilation of the isopycnal of $\sigma = 26 \text{ kg/m}^3$ above the outer shelf. In July, a large tongue of cold water propagates slantwise below the newly formed pycnocline between the isopycnal layers of $\sigma = 26 - 27 \text{ kg/m}^3$, while mixing and cascading of denser waters is still evident along the shelf break. In December 2002, water structure nearly repeats the transect in December 2001.

Examples of the reproduction of observed cascading events, at the same location and time (see also Figure S3), gives us confidence that, despite the modest horizontal resolution, this model performs satisfactorily in the direct simulation of cascading. Thus, estimates of cascading fluxes, discussed previously (see section 5), can be seen as reliable first-order estimates.

5.4. Cascading and the Pathways of Pacific Waters

To obtain more spatial details on the DWC event in July 2002 in the Chukchi Sea and to examine the spread of Pacific Water in the Canadian Basin, we analyze the pathways of trajectories originated in the Bering Strait with the use of the output of the 1/12° global model (see section 3.2). Figure 13 shows the 1/12° model temperature (a) and salinity (b) fields in the Canadian Basin at ~100 m, as well as the depth of trajectories of the Pacific Water tracers. The temperature and salinity fields are evidence of the cold (at about freezing point) and saline (up to 33.5) waters cascading from the shelf following the canyons (Herald, the Barrow Canyons, and the smaller canyons, e.g., a deep extension of Central Channel) and then spreading eastward (clockwise, anticyclonically) and offshore in the Canada Basin. This pattern has been suggested by the observational transects completed on the western Chukchi shelf (e.g., Pickart et al., 2009, 2010). The Barrow Canyon also has a signature of westward propagating cold waters at 100 m.

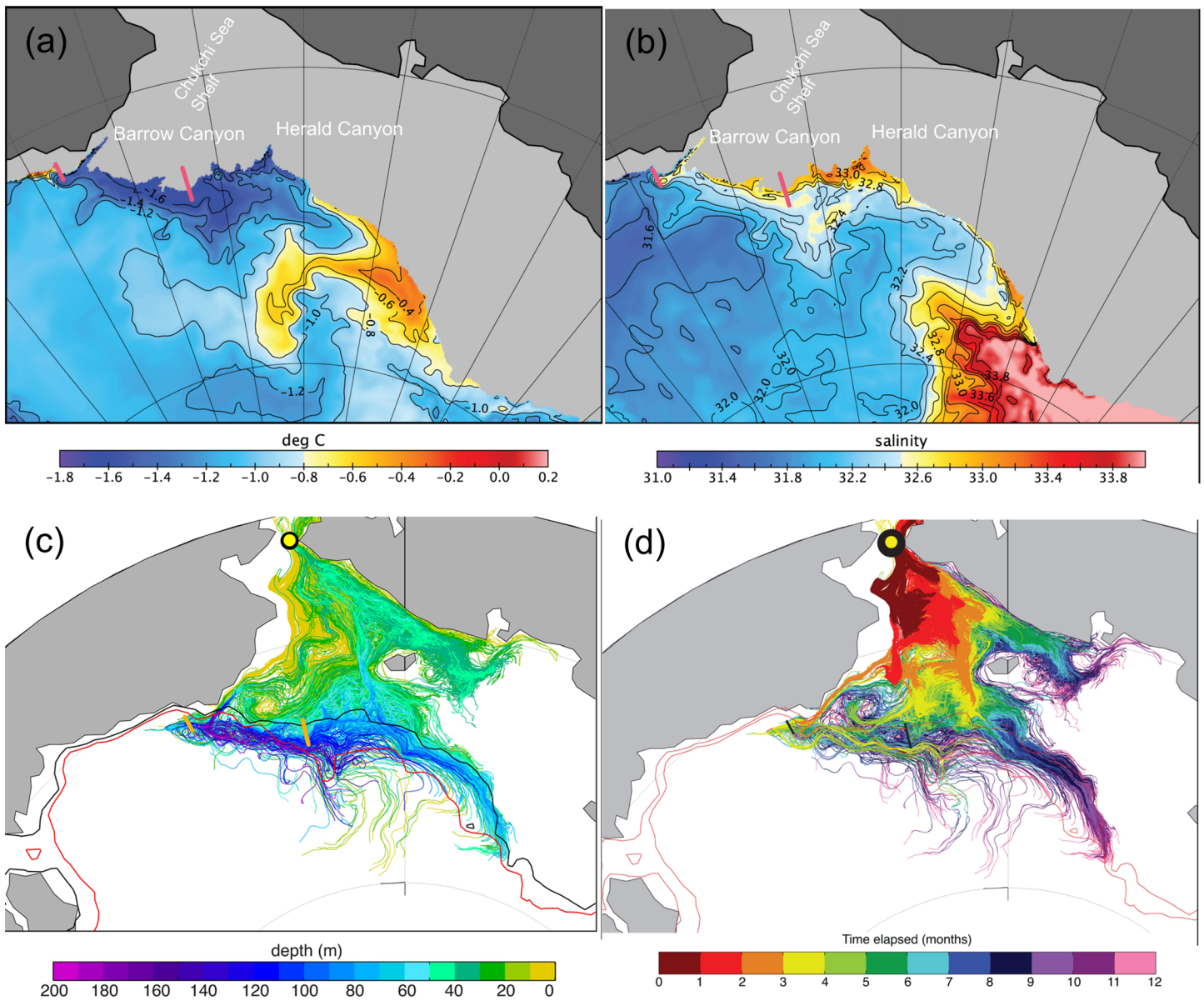


Figure 13. (a) Temperature at the depth of 100 m in simulations of 1/12° global NEMO and (b) trajectories of Lagrangian particles (see section 3.2 for description) and the depth of particles are displayed by color: Purples are plotted over greens to highlight the deepest part of trajectories. Isobaths at 100 and 300 m are shown by green and yellow contours, and locations of Barrow and Herald Canyons are shown by yellow circles in (b). (c) Salinity at 100 m and (d) advective pathways and time scales associated with these releases, with reds plotted on top of blues to highlight the most rapid pathways shelf break (red contours). Locations of transects discussed in Pickart et al. (2010) are shown.

The particle tracking experiments show Pacific water crossing the shelf in several branches during 3–4 months. The water meanders on the shelf and then descends to a depth of 160–200 m in the deep Canada basin (Figures 13c and 13d), moving clockwise. Descending water was formed during winter, thus the deepening stage would correspond to middle and late summer (July–September). Note that the deepest trajectories propagating across the Chukchi shelf, and nearly corresponding to the depth of the shelf at these locations (Figure 13c), coincide with the maximum of MLD salinity seen in Figure 7 (see also Movie S1). The locations of cold and saline water at the depth of 100 m in July 2000 (Figures 13a and 13b) correspond well with the preconditioning shown in Figure 7. Thus, both regional and global models, with different horizontal and vertical resolutions, demonstrate similar results.

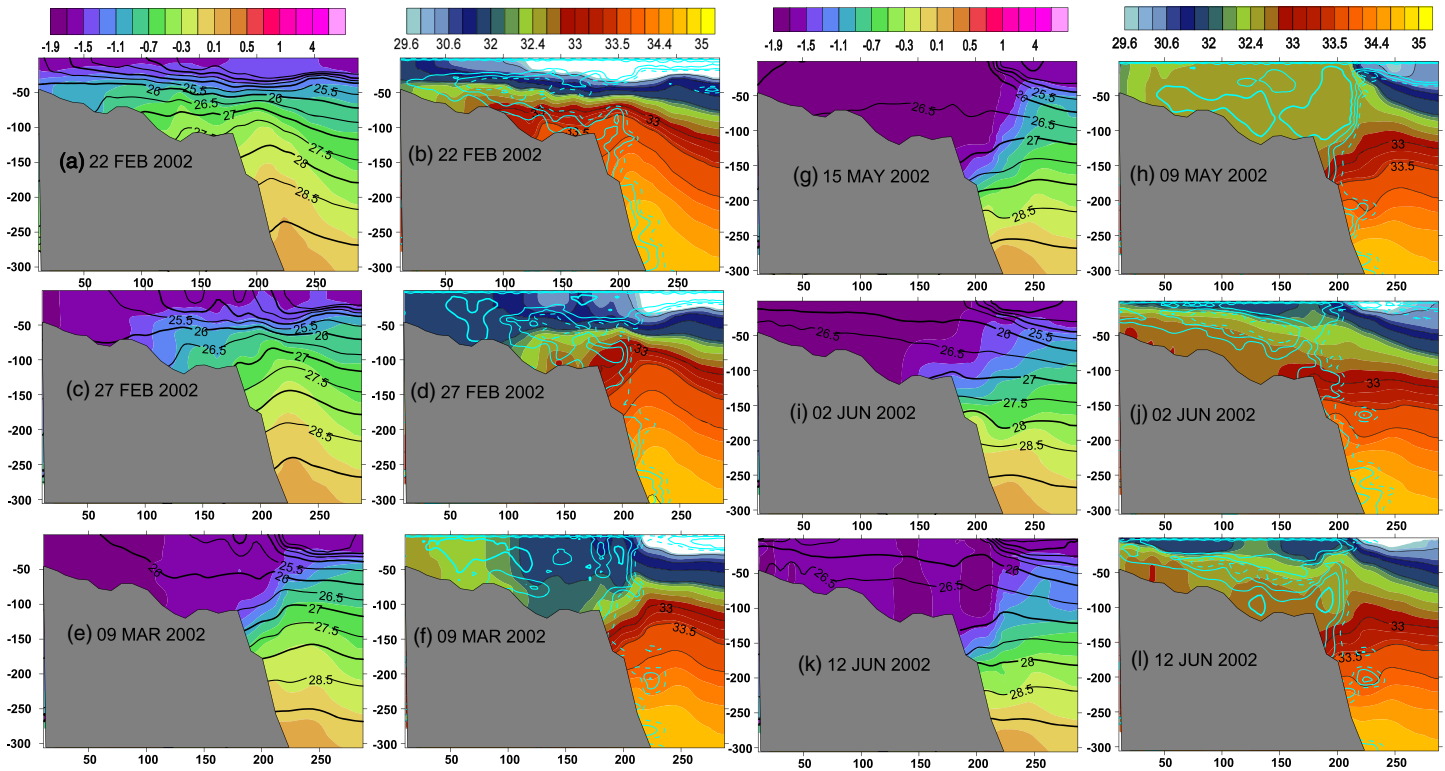


Figure 14. Transects (a, c, e, g, i, k) of potential temperature, potential density (in σ units), and (b, d, f, h, j, l) salinity and vertical diffusivity K_{vT} along the transect in the Barrow Canyon (shown in Figure 7) at different time at 2002: (a, b) 22 February, (c, d) 27 February, (e, f) 9 March, (g, h) 15 May, (i, j) 2 June, and (k, l) 12 June. Temperature and salinity are shown by color, density is shown by black contours, $\log_{10}K_{vT} = (-3, 2) \text{ m}^2/\text{s}$ is shown by blue solid line, and $\log_{10}K_{vT} = -4 \text{ m}^2/\text{s}$ is shown by dashed blue line. Note that the background value of vertical diffusivity is $10^{-6} \text{ m}^2/\text{s}$.

The question that arises is does the upwelling observed at the 166°W transects and at the other locations support cascading and mixing of waters of Pacific and Atlantic origin? If so, is it a repeating feature? Autumn upwelling, associated with storms crossing the western Chukchi and Beaufort Seas, is a common feature of the Canadian Arctic dynamics (Pickart et al., 2009). Indeed, all the Lagrangian trajectories originated on the surface on the Bering Strait, tracing the waters with very low salinity. However, after water modification due to brine rejection and cooling, or mixing, the trajectories become dense enough to reach depths below 160–200 m. To support this conclusion, we present an animation (Movie S4) of potential temperature, density, and vertical diffusivity, simulated with the regional pan-Arctic model, at a transect along the 100-m isobaths (contour and key locations are shown in Figure 7). This animation demonstrates yearly repeatable upwelling of warm dense waters onto the shelf during October–November. At some locations, strong diapycnal mixing, exceeding the background by 3–4 orders of magnitude, results in the cooling of the mixed waters and the ventilation of isopycnals.

The Barrow and Herald canyons are suggested to be the main gateways for the passage of Pacific waters (Pickart et al., 2009; Spall et al., 2008; Figure 1), which is supported by modeled trajectories (Figure 13). To examine the interaction of upwelling and cascading in more detail, we consider time slices at transects along Barrow and Herald Canyons, shown in Figure 7.

Strong upwelling of warmer and saltier waters is evident in the Barrow Canyon in February 2002 (Figures 14a and 14b), penetrating up to a depth of 50 m and distance of 200 km from the base of Barrow Canyon. These waters are separated from the cold ($T \sim -1.9^\circ\text{C}$, -1.5°C) and fresh surface ($S < 29.5 - 30$ PSU) waters by a strong halocline. Just a week later, cooling and ventilation start at the shallowest part of the canyon, accompanied by strong vertical mixing in the intermediate layers (Figures 14c and 14d). In early March (Figures 14d and 14e), mixed waters on the shelf become colder and fresher but less dense ($\sigma \approx 26 - 26.5 \text{ kg/m}^3$) compared with the stratified waters in the deeper part of the basin (at 100 m; $\sigma \approx 26.5 - 27 \text{ kg/m}^3$), while cooling by $0.3\text{--}0.5^\circ\text{C}$ of the layer ($\sigma \approx 26.5 - 27.5 \text{ kg/m}^3$) at the shelf break

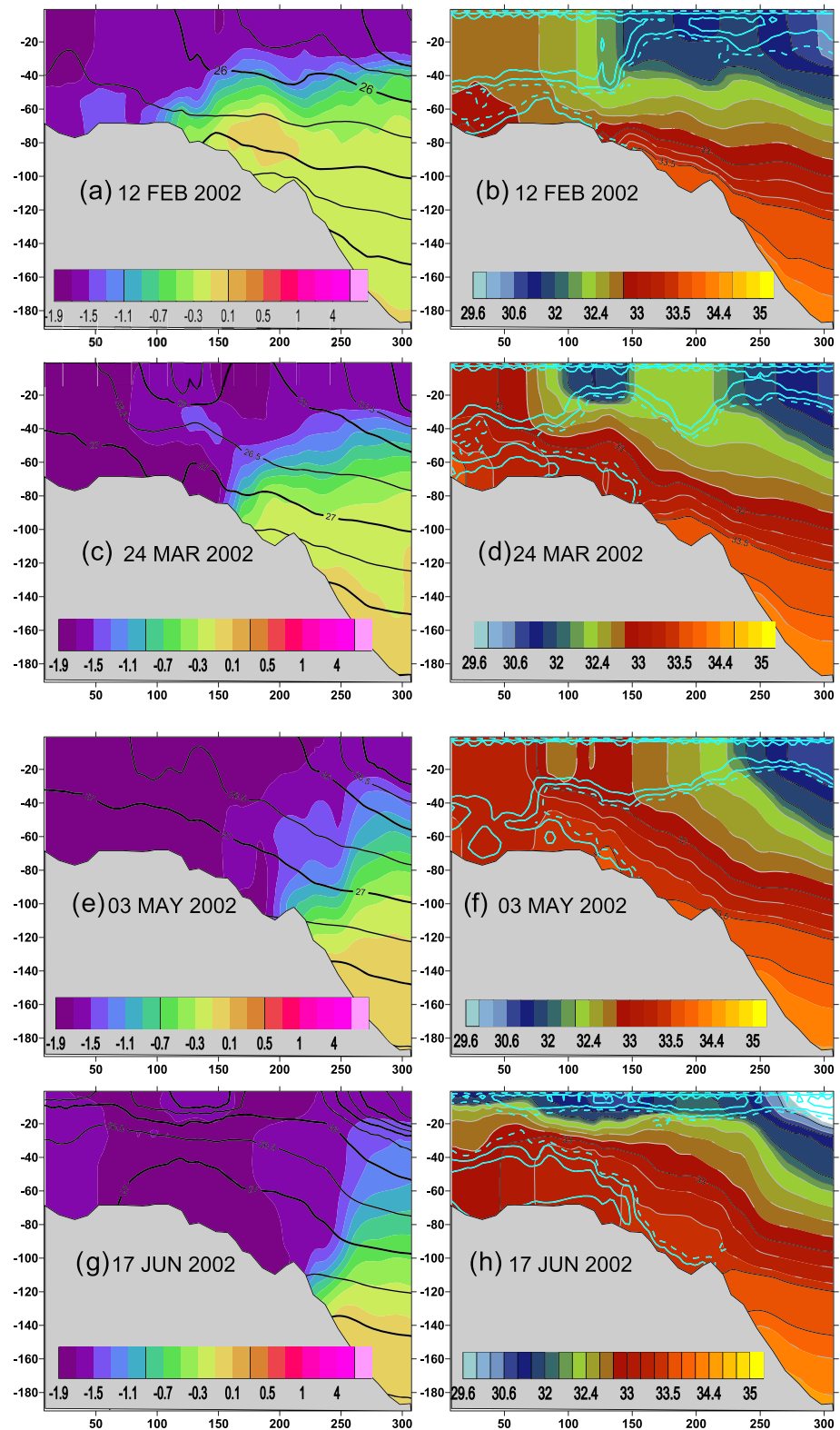


Figure 15. Transects (a, c, e, g) of potential temperature and density (in σ units) and (b, d, f, h) salinity and vertical diffusivity K_{vT} along the Barrow Canyon (see locations at Figure 7) at different time at 2002: (a, b) 12 February, (c, d) 24 March, (e, f) 3 May, and (g, h) 17 June. Temperature and salinity are shown by color, density is shown by black contours, $\log_{10}K_{vT} = (-3, 2) \text{ m}^2/\text{s}$ is shown by blue solid line, and $\log_{10}K_{vT} = -4 \text{ m}^2/\text{s}$ is shown by dashed blue line. Note that the background value of vertical diffusivity is $10^{-6} \text{ m}^2/\text{s}$.

become evident. Cooling and loss of buoyancy on the shelf and at the edge of the shelf break continue up to May (Figures 14g and 14h), with a cascading plume penetrating to a depth of 150 m on the steep slope and a vertical diffusivity in the plume exceeding $10^{-3} \text{ m}^2/\text{s}$ (Figure 14h). Cooling due to entrainment and vertical mixing is extended up to a depth of 180 m, corresponding to the $\sigma \approx 27.5 \text{ kg/m}^3$ isopycnal and $S \approx 33.5$ PSU isohaline, which is 0.5 – 0.8 PSU more saline than the mixed waters on the shelf. Note that, according to Movie S3 and Figure 13, these waters propagate westward being replaced by the cascading shelf waters. Two weeks later (2 June; Figures 14i and 14j), local upwelling uplifts warmer saltier waters back to a depth of 80–100 m, accompanied by strong vertical mixing (diffusivity $10^{-2} \text{ m}^2/\text{s}$). At this time a strong summer seasonal halocline starts to form, preventing the mixing between subsurface and benthic layers. Ten days later, in the middle of June (Figures 14k and 14l), colder waters ($T \approx -1\text{C}^\circ$) propagate downslope to the depth of 150 m. The combination of upwelling and cascading in the Barrow Canyon is evident from Figures 9d–9f, with signals of synoptic-scale variability in the upwelling events.

Autumn-winter upwelling of warmer and saltier waters on the shelf is a remarkable feature in the Herald Canyon (22 February, 2002; Figures 15a and 15b), uplifting saltier and warmer ($S \approx 33 - 33.5$ PSU, $T \approx -0.3, +0.2\text{C}^\circ$) waters to the shelf up to a depth of 70 m. Brine rejection and cooling in the shallow part of the Canyon result in the surface ventilation of the 33 PSU isohaline by the end of March (Figures 15c and 15d; at the distance 0–50 km), while cooling of the warm, saline tongue (Figure 15a; at the distance ~120–150 km) forms a blob of water denser than $\sigma \approx 27 \text{ kg/m}^3$ (Figure 15c). A cold front propagates downslope and reaches a depth of 100 m by the middle of June. The propagation of well-mixed waters and shape of the cascading tongue is highlighted by the high vertical diffusivity contour (blue solid lines in Figures 15b, 15d, 15f, and 15h). At this time, the benthic and surface mixed layer are separated by a newly formed halocline due to melting of ice at the surface, which is in accordance with Movie S3.

Thus, our simulations support the hypothesis that upwelling and vertical mixing with uplifted Atlantic Waters are likely mechanisms amplifying the formation of heavy dense waters and presumably increasing ventilation of intermediate and deep waters. Deeper (500–1,000 m) and stronger ($>1 \text{ m}^2/\text{s}$) DWC fluxes are simulated in the Chukchi Plateau (Figures 3a and 3b).

6. Summary

The process of DWC, a specific type of topographically trapped flow originating on the shelf, plays a particularly important role in the Arctic Ocean. It is the principal mechanism of ventilation whereby intermediate and deep waters are replenished. DWC events can also contribute to the export and storage of carbon from the shelf as a constituent of the “shelf carbon pump” (Holt et al., 2009) and have been shown to contribute to the modification of Atlantic water (Ivanov & Golovin, 2007). The export of water from the shelf can induce a compensating flow of the deep water onto the shelf (Ivanov & Golovin, 2007; Kämpf, 2005), with the potential to provide a supply of nutrients to the upper ocean and to affect primary production. DWC events are hard to observe due to their sporadic nature and the technical difficulties of obtaining wintertime observations under sea ice. Until now, to our knowledge, only 27 locations of cascading in the Arctic Ocean have been reported in the literature. There have also been few regional modeling studies examining cascading events in the Arctic Ocean: Previous examples include Ivanov and Golovin (2007), Ivanov et al. (2015), Marson et al. (2017), Wobus et al. (2013), and Magaldi and Haine (2015).

In this work a pan-Arctic ocean-ice coupled model, with moderate horizontal grid spacing (10–15 km) and fine vertical discretization (0.3–3 m) resolving shelf slopes, is used to examine the ability of 3-D general circulation models to reproduce these observed cascading events and to diagnose their importance on a pan-Arctic scale. Given the choice between fine vertical and fine horizontal resolution for this simulation, we here opted to focus on fine vertical resolution to capture the dominant benthic layer processes at the expense of topographic detail and their interaction with the mesoscale eddies. Using a 30-year simulation, we analyzed model output to detect the most favorable locations of DWC (see Figure 3). We found that most of the locations of the observed DWC events (cf. Figure 1) are reproduced by the model.

The shelf-slope areas around the Canadian Basin provided the focus for a detailed comparison of model results with observations. The present-day sea ice seasonal cycle in the North American Arctic shelf seas, with extended summertime ice-free areas and complete ice coverage in winter, favors pre-conditioning of

Acknowledgments

The research presented in this paper was conceived and led by Dr. Maria Luneva. Tragically, she passed away in March 2020. Maria has inspired many colleagues in different countries across the world with her enthusiasm for taking on scientific challenges and her devotion to science. All the Maria's colleagues and friends will greatly miss her open friendly personality and her scientific insights. The authors dedicate this paper to Maria's memory. The authors acknowledge the National Capability funding in the CLASS programme by the U.K. Natural Environment Research Council (NERC) (grant NE/R015953/1), NERC sponsored program ORCHESTRA (grant NE/N018095/1), the NERC-BMBF project "Advective pathways of nutrients and key ecological substances in the Arctic: APEAR" (grant NE/R012865/1), under the UK-Germany Changing Arctic Ocean Programme, the NERC project "Preconditioning the trigger for rapid Arctic ice melt: PRE-MELT" (grant NE/T000260/1) and the NERC LTS-M "Atlantic Climate System Integrated Study Programme (ACSIS)," (grant NE/N018044/1). The authors are grateful for the financial support from the UK Arctic Office Bursary "Contribution of eddies and dense water cascading to cross-shelf exchange" for making the international exchanges and research co-operation possible. Vladimir Ivanov and Fedor Tuzov acknowledge financial support from the Russian Science Foundation, Grant 19-17-00110. We also thank AOMIP and the Forum for Arctic Ocean Modeling and Observational Synthesis (FAMOS), funded by the National Science Foundation Office of Polar Programs (Awards PLR-1313614 and PLR-1203720), for providing travel support to attend the FAMOS workshops and for a great opportunity to develop and share ideas on Arctic research. We thank the anonymous reviewers for the thorough and kind comments which helped to make the manuscript better. We also acknowledge use of the U.K. National High Performance Computing resource (<http://www.archer.ac.uk>).

DWC events. The results reveal that the model, despite its relatively coarse horizontal resolution, has the capability to simulate DWC events, or at least intense shelf convection, in most of these cases. Therefore, the trend of increasing cascade intensity under conditions of enhanced seasonality of the Arctic sea ice cover, revealed in the model simulation, may be taken as a plausible projection for the near future.

Examining the conditions and preconditions of DWC in the western Chukchi Sea (Figures 12–14), we found that active DWCs are preceded by autumn upwelling and uplifting of the Atlantic warm and saltier waters on the shelf. Upwelling associated with storm tracks is a frequently observed feature in this region (Pickart et al., 2009). The simulation shows the presence of active diapycnal mixing and cooling of uplifted waters, resulted in the formation of denser waters, able to descend to depths as large as 160–200 m. Therefore, these simulations support the hypothesis by Aagaard et al. (1981). The Pacific water Lagrangian experiments (see sections 3.2 and 5.4 and Figure 13) suggest a counterclockwise initial spread of the cascading waters next to the shelf slope, with a change of pathways to clockwise in the deep Canada Basin, at about 160- to 200-m depth. The time scale for the winter Pacific water to cross the shelf and the deep Arctic Ocean is about 3–4 months.

We provide the first model-based estimates of the various components of shelf-ocean transport fluxes in the deep Arctic Ocean and seas of the Northern Atlantic Ocean connected to the Arctic (Figure 6): DWC and SEF and BEF. Specifically, the 25-year mean exchange in the "Deep Arctic" (Regions 6 to 12 in Figure 1) across the 300-m isobath is dominated by a DWC flux of 1.3 Sv compared with 0.85 Sv for SEF and 0.58 Sv for BEF. Thus, the simulated DWC flux is comparable to the total Bering Strait inflow (0.8–1.3 Sv). Finally, in most sections along the 300-m isobath, the most intense cascading happens during mid-January to February (Figure 6). This would imply that the cascading events detected in observations, mostly in ice-free conditions in September–October, underestimate the actual intensity of such events.

Simulated cascading fluxes bring colder waters to the ocean interior, with 25-year mean maximal negative vertically integrated heat flux anomalies (per unit length along the 300-m isobath) exceeding $4\text{--}10 \times 10^6$ W/m in the Irminger Sea, Barents Seas, and near the North-East Greenland shelf break (Figure 4g).

Interannual variability of DWC flux in the "Deep Arctic" is strong, with relative anomalies reaching 50% (~1.6 Sv in 1993 and 2008 vs. 0.8 Sv before 1990 and in winter 2004–2005) (Figure 7c), and does not correlate directly with the phase of Arctic Ocean Oscillation index (Proshutinsky et al., 2015). However, the SEF and DWC have positive trends with time, 0.023 and 0.0175 Sv/year, presumably caused by summer ice decline (Figures 7a and 7b).

Data Availability Statement

Baseline model is a regional configuration of NEMO (Nucleus for European Models of the Ocean), at Version 3.6 stable (Madec & NEMO team, 2016). Model code (Version 3.6 stable) is available from the NEMO website (www.nemo-ocean.eu). Model output, used in this study, is now under archiving process at British Oceanographic Data Centre (BODC, <https://www.bodc.ac.uk/>).

References

- Aagaard, K., Coachman, L. K., & Carmack, E. (1981). On the halocline of the Arctic Ocean. Deep Sea Research Part A. *Oceanographic Research Papers*, 28(6), 529–545. [https://doi.org/10.1016/0198-0149\(81\)90115-1](https://doi.org/10.1016/0198-0149(81)90115-1)
- Aagaard, K., & Roach, A. T. (1990). Arctic ocean-shelf exchange: Measurements in Barrow Canyon. *Journal of Geophysical Research*, 95(C10), 18,163–18,175. <https://doi.org/10.1029/JC095iC10p18163>
- Aksenov, Y., Bacon, S., Coward, A. C., & Nurser, A. G. (2010). The North Atlantic inflow to the Arctic Ocean: High-resolution model study. *Journal of Marine Systems*, 79(1–2), 1–22. <https://doi.org/10.1016/j.jmarsys.2009.05.003>
- Aksenov, Y., Ivanov, V. V., Nurser, A. G., Bacon, S., Polyakov, I. V., Coward, A. C., et al. (2011). The Arctic circumpolar boundary current. *Journal of Geophysical Research*, 116, C09017. <https://doi.org/10.1029/2010JC006637>
- Aksenov, Y., Karcher, M., Proshutinsky, A., Gerdes, R., De Cuevas, B., Golubeva, E., et al. (2016). Arctic pathways of Pacific Water: Arctic Ocean Model Intercomparison experiments. *Journal of Geophysical Research: Oceans*, 121, 27–59. <https://doi.org/10.1002/2015JC011299>
- Aksenov, Y., Popova, E. E., Yool, A., Nurser, A. G., Williams, T. D., Bertino, L., & Bergh, J. (2017). On the future navigability of Arctic Sea routes: High-resolution projections of the Arctic Ocean and sea ice. *Marine Policy*, 75, 300–317. <https://doi.org/10.1016/j.marpol.2015.12.027>
- Armitage, T. W. K., Bacon, S., Ridout, A. L., Thomas, S. F., Aksenov, Y., & Wingham, D. J. (2016). Arctic sea surface height variability and change from satellite radar altimetry and GRACE, 2003–2014. *Journal of Geophysical Research: Oceans*, 121, 4303–4322. <https://doi.org/10.1002/2015JC011579>

- Bacon, S., Aksenov, Y., Fawcett, S., & Madec, G. (2015). Arctic mass, freshwater and heat fluxes: Methods and modelled seasonal variability. *Philosophical Transactions of the Royal Society A: Mathematical, Physical and Engineering Sciences*, 373(2052), 20140169. <https://doi.org/10.1098/rsta.2014.0169>
- Bacon, S., Marshall, A., Holliday, N. P., Aksenov, Y., & Dye, S. R. (2014). Seasonal variability of the East Greenland coastal current. *Journal of Geophysical Research: Oceans*, 119, 3967–3987. <https://doi.org/10.1002/2013JC009279>
- Bamber, J., van den Broeke, M., Ettema, J., Lenaerts, J., & Rignot, E. (2012). Recent large increases in freshwater fluxes from Greenland into the North Atlantic. *Geophysical Research Letters*, 39, L19501. <https://doi.org/10.1029/2012GL052552>
- Bareiss, J., & Görge, K. (2005). Spatial and temporal variability of sea ice in the Laptev Sea: Analyses and review of satellite passive-microwave data and model results, 1979 to 2002. *Global and Planetary Change*, 48(1–3), 28–54. <https://doi.org/10.1016/j.gloplacha.2004.12.004>
- BarKode. Oceanographic database (CD-ROM) (1999). *Data of the BarKode CD-ROM provided by the International ACSYS/CLIM*. Murmansk/Tromsø: IACPO Informal Report No. 5. Retrieved from http://www.climate-cryosphere.org/media-gallery/289-iacpo-inf-05?album_id=39
- Blanke, B., & Delecluse, P. (1993). Low frequency variability of the tropical Atlantic Ocean simulated by a general circulation model with mixed layer physics. *Journal of Physical Oceanography*, 23(7), 1363–1388. [https://doi.org/10.1175/1520-0485\(1993\)023<1363:VOTTAO>2.0.CO;2](https://doi.org/10.1175/1520-0485(1993)023<1363:VOTTAO>2.0.CO;2)
- Blanke, B., & Raynaud, S. (1997). Kinematics of the Pacific equatorial undercurrent: An Eulerian and Lagrangian approach from GCM results. *Journal of Physical Oceanography*, 27(6), 1038–1053. [https://doi.org/10.1175/1520-0485\(1997\)027<1038:KOTPEU>2.0.CO;2](https://doi.org/10.1175/1520-0485(1997)027<1038:KOTPEU>2.0.CO;2)
- Bouillon, S., Maqueda, M. A. M., Legat, V., & Fichefet, T. (2009). An elastic–viscous–plastic sea ice model formulated on Arakawa B and C grids. *Ocean Modelling*, 27(3–4), 174–184. <https://doi.org/10.1016/j.ocemod.2009.01.004>
- Bruciaferri, D., Shapiro, G. I., & Wobus, F. (2018). A multi-envelope vertical coordinate system for numerical ocean modelling. *Ocean Dynamics*, 68(10), 1239–1258. <https://doi.org/10.1007/s10236-018-1189-x>
- Canuto, V. M., Howard, A., Cheng, Y., & Dubovikov, M. S. (2001). Ocean turbulence. Part I: One-point closure model—Momentum and heat vertical diffusivities. *Journal of Physical Oceanography*, 31(6), 1413–1426. [https://doi.org/10.1175/1520-0485\(2001\)031<1413:OTPIOP>2.0.CO;2](https://doi.org/10.1175/1520-0485(2001)031<1413:OTPIOP>2.0.CO;2)
- Cavaleri, D. J., & Martin, S. (1994). The contribution of Alaskan, Siberian, and Canadian coastal polynyas to the cold halocline layer of the Arctic Ocean. *Journal of Geophysical Research*, 99(C9), 18,343–18,362. <https://doi.org/10.1029/94JC01169>
- Chapman, D. C., & Gawarkiewicz, G. (1995). Offshore transport of dense shelf water in the presence of a submarine canyon. *Journal of Geophysical Research*, 100(C7), 13,373–13,387. <https://doi.org/10.1029/95JC00890>
- Colombo, P. (2018). *Modélisation des écoulements d'eaux denses à travers des seuils topographiques dans les modèles réalistes de circulation océanique: une démonstration du potentiel que représente l'hybridation d'une coordonnée géopotentielle et d'une coordonnée suivant le terrain*. Sciences de la Terre: Université Grenoble Alpes, Français. NNT: 2018GREAU017.
- Colombo, P., Barnier, B., Penduff, T., Chanut, J., Deshayes, J., Molines, J.-M., et al. (2020). Representation of the Denmark Strait overflow in a z-coordinate eddy configuration of the NEMO (v3.6) ocean model: Resolution and parameter impacts. *Geoscientific Model Development*. <https://doi.org/10.5194/gmd-2019-272>
- Condie, S. A. (1995). Descent of dense water masses along continental slopes. *Journal of Marine Research*, 53(6), 897–928. <https://doi.org/10.1357/0022240953212936>
- Dai, A., Qian, T., Trenberth, K. E., & Milliman, J. D. (2009). Changes in continental freshwater discharge from 1948–2004. *Journal of Climate*, 22(10), 2773–2792. <https://doi.org/10.1175/2008JCLI2592.1>
- Dmitrenko, I. A., Kirillov, S. A., Ivanov, V. V., Woodgate, R. A., Polyakov, I. V., Koldunov, N., et al. (2009). Seasonal modification of the Arctic Ocean intermediate water layer off the eastern Laptev Sea continental shelf break. *Journal of Geophysical Research*, 114, C06010. <https://doi.org/10.1029/2008JC005229>
- DRAKKAR (2012). *Coordination of high resolution global ocean simulations and developments of the NEMO Modelling Framework*. Coordinators: Treguer A. Barnier: http://www.drakkar-ocean.eu/publications/reports/reports-of-activity-french-drakkar-team/report_drakkar_lefe_2010-2012_final.pdf
- Egbert, G. D., & Erofeeva, S. Y. (2002). Efficient inverse modeling of barotropic ocean tides. *Journal of Atmospheric and Oceanic Technology*, 19(2), 183–204. [https://doi.org/10.1175/1520-0426\(2002\)019<0183:EIMOBO>2.0.CO;2](https://doi.org/10.1175/1520-0426(2002)019<0183:EIMOBO>2.0.CO;2)
- Ezer, T., & Mellor, G. L. (2004). A generalized coordinate ocean model and a comparison of the bottom boundary layer dynamics in terrain-following and in z-level grids. *Ocean Modelling*, 6(3–4), 379–403. [https://doi.org/10.1016/S1463-5003\(03\)00026-X](https://doi.org/10.1016/S1463-5003(03)00026-X)
- Falina, A., Sarafanov, A., Mercier, H., Lherminier, P., Sokov, A., & Danialt, N. (2012). On the cascading of dense shelf waters in the Irminger Sea. *Journal of Physical Oceanography*, 42(12), 2254–2267. <https://doi.org/10.1175/JPO-D-12-012.1>
- Fichefet, T., & Maqueda, M. M. (1997). Sensitivity of a global sea ice model to the treatment of ice thermodynamics and dynamics. *Journal of Geophysical Research*, 102(C6), 12,609–12,646. <https://doi.org/10.1029/97JC00480>
- Flather, R. A. (1976). A tidal model of the northwest European continental shelf. *Memoires de la Societe Royale des Sciences de Liege*, 10, 141–164.
- Gammelsrod, T., Leikvin, Ø., Lien, V., Budgell, W. P., Loeng, H., & Maslowski, W. (2009). Mass and heat transports in the NE Barents Sea: Observations and models. *Journal of Marine Systems*, 75, 56–69. <https://doi.org/10.1016/j.jmarsys.2008.07.010>
- Gavilan Pascual-Ahuir, E., Willmott, A. J., Maqueda, M. M., & Luneva, M. V. (2020). Topographical control of the source-sink and wind stress driven planetary geostrophic circulation in a polar basin. *Journal of Geophysical Research: Oceans*, 125, e2019JC015571. <https://doi.org/10.1029/2019JC015571>
- Gill, A. E. (1968). Similarity theory and geostrophic adjustment. *Quarterly Journal of the Royal Meteorological Society*, 94(402), 586–588. <https://doi.org/10.1002/qj.49709440214>
- Golovin, P. N. (2005). Formation and sink of dense shelf waters in the area of the continental slope (cascading) of the Nansen Basin in the Laptev Sea. *Russian Meteorology and Hydrology*, 30(1), 33–47. https://www.researchgate.net/publication/292836415_Formation_and_sink_of_dense_shelf_waters_in_the_area_of_the_continental_slope_cascading_of_the_Nansen_Basin_in_the_Laptev_Sea
- Harden, B. E., Pickart, R. S., & Renfrew, I. A. (2014). Offshore transport of dense water from the East Greenland shelf. *Journal of Physical Oceanography*, 44(1), 229–245. <https://doi.org/10.1175/JPO-D-12-0218.1>
- Hirano, D., Fukamachi, Y., Watanabe, E., Ohshima, K. I., Iwamoto, K., Mahoney, A. R., et al. (2016). A wind-driven, hybrid latent and sensible heat coastal polynya off Barrow, Alaska. *Journal of Geophysical Research: Oceans*, 121, 980–997. <https://doi.org/10.1002/2015JC011318>
- Holt, J., Wakelin, S., & Huthnance, J. M. (2009). Down-welling circulation of the north west European continental shelf: A driving mechanism for the continental shelf carbon pump. *Geophysical Research Letters*, 36, L14602. <https://doi.org/10.1029/2009GL038997>

- Hunke, E. C., & Dukowicz, J. K. (1997). An elastic–viscous–plastic model for sea ice dynamics. *Journal of Physical Oceanography*, 27(9), 1849–1867. <https://doi.org/10.1175/1520-0485>
- Huthnance, J. M. (1995). Circulation, exchange and water masses at the ocean margin: The role of physical processes at the shelf edge. *Progress in Oceanography*, 35(4), 353–431. [https://doi.org/10.1016/0079-6611\(95\)80003-C](https://doi.org/10.1016/0079-6611(95)80003-C)
- Huthnance, J. M. (2009). Accelerating dense water flow down a slope. *Journal of Physical Oceanography*, 39(6), 1495–1511. <https://doi.org/10.1175/2008JPO3964.1>
- Ivanov, V., Alexeev, V., Koldunov, N. V., Repina, I., Sandø, A. B., Smedsrud, L. H., & Smirnov, A. (2016). Arctic Ocean heat impact on regional ice decay: A suggested positive feedback. *Journal of Physical Oceanography*, 46(5), 1437–1456. <https://doi.org/10.1175/JPO-D-15-0144.1>
- Ivanov, V. V., & Golovin, P. N. (2007). Observations and modeling of dense water cascading from the northwestern Laptev Sea shelf. *Journal of Geophysical Research*, 112, C09003. <https://doi.org/10.1029/2006JC003882>
- Ivanov, V. V., Maslov, P., Aksenov, Y., & Coward, A. (2015). Shelf-basin exchange in the Laptev Sea in the warming climate: A model study. *Geophys. & Astrophys. Fluid Dynamics*, 109(3), 254–280. <https://doi.org/10.1080/03091929.2015.1025776>
- Ivanov, V. V., & Repina, I. A. (2019). Mid-winter anomaly of sea ice in the Western Nansen Basin in 2010s. *IOP Conf. Ser. Earth and Environmental Science*, 231, 012024. <https://doi.org/10.1088/1755-1315/231/1/012024>
- Ivanov, V. V., Shapiro, G. I., Huthnance, J. M., Aleynik, D. L., & Golovin, P. N. (2004). Cascades of dense water around the world ocean. *Progress in Oceanography*, 60(1), 47–98. <https://doi.org/10.1016/j.pocean.2003.12.002>
- Ivanov, V. V., & Watanabe, E. (2013). Does Arctic sea ice reduction foster shelf–basin exchange? *Ecological Applications*, 23(8), 1765–1777. <https://doi.org/10.1890/11-1069.1>
- Kämpf, J. (2005). Cascading-driven upwelling in submarine canyons at high latitudes. *Journal of Geophysical Research*, 110, C02007. <https://doi.org/10.1029/2004JC002554>
- Kelly, S., Popova, E., Aksenov, Y., Marsh, R., & Yool, A. (2018). Lagrangian modeling of Arctic Ocean circulation pathways: Impact of advection on spread of pollutants. *Journal of Geophysical Research: Oceans*, 123, 2882–2902. <https://doi.org/10.1002/2017JC013460>
- Kelly, S. J., Popova, E., Aksenov, Y., Marsh, R., & Yool, A. (2020). They came from the Pacific: How changing Arctic currents could contribute to an ecological regime shift in the Atlantic Ocean. *Earth's Future*, 8, e2019EF001394. <https://doi.org/10.1029/2019EF001394>
- Koenig, Z., Meyer, A., Provost, C., Sennéchal, N., Sundfjord, A., Beguery, L., et al. (2018). Cooling and freshening of the West Spitsbergen Current by shelf-origin cold core lenses. *Journal of Geophysical Research: Oceans*, 123, 8299–8312. <https://doi.org/10.1029/2018JC014463>
- Kwok, R., Cunningham, G. F., Wensnahan, M., Rigor, I., Zwally, H. J., & Yi, D. (2009). Thinning and volume loss of the Arctic Ocean sea ice cover: 2003–2008. *Journal of Geophysical Research*, 114, C07005. <https://doi.org/10.1029/2009JC005312>
- Large, W. G., & Yeager, S. G. (2004). *Diurnal to decadal global forcing for ocean and sea-ice models: The data sets and flux climatologies*. Boulder, CO: Climate and global dynamics division, national center for atmospheric research Boulder, Colorado.
- Legg, S., Briegleb, B., Chang, Y., Chassignet, E. P., Danabasoglu, G. D., Ezer, T., et al. (2009). Improving oceanic overflow representation in climate models. *Bulletin of the American Meteorological Society*, 657–669. <https://doi.org/10.1175/2008bams2667.1>
- Lind, S., Ingvaldsen, R. B., & Furevik, T. (2018). Arctic warming hotspot in the northern Barents Sea linked to declining sea-ice import. *Nature Climate Change*, 8(7), 634–639. <https://doi.org/10.1038/s41558-018-0205-y>
- Luneva, M. V., Aksenov, Y., Harle, J. D., & Holt, J. T. (2015). The effect of tides on the water mass mixing and sea ice in the Arctic Ocean. *Journal of Geophysical Research: Oceans*, 120, 6669–6699. <https://doi.org/10.1002/2014JC010310>
- Madec, G., & NEMO Team (2016). *NEMO reference manual 3.6_STABLE: “NEMO ocean engine” Note du Pole de modélisation*. Paris, France: Inst. Pierre-Simon Laplace (IPSL). No 27 ISSN 1288-1619 Retrieved from https://www.nemo-ocean.eu/wp-content/uploads/NEMO_book.pdf
- Madec, G. V. (2008). *NEMO Ocean engine. Laboratoire d’Océanographie et du Climat: Expérimentation et Approches Numeriques*. Paris, France. Retrieved from <https://www.nemo-ocean.eu>
- Magaldi, M. G., & Haine, T. W. N. (2015). Hydrostatic and non-hydrostatic simulations of dense waters cascading off the shelf: The East Greenland case. *Deep Sea Research, Part I*, 96, 89–104. <https://doi.org/10.1016/j.dsr.2014.10.008>
- Marshall, J., & Schott, F. (1999). Open-ocean convection: Observations, theory, and models. *Reviews of Geophysics*, 37(1), 1–64. <https://doi.org/10.1029/98RG02739>
- Marson, J. M., Myers, P. G., Hu, X., Petrie, B., Azetsu-Scott, K., & Lee, C. M. (2017). Cascading off the West Greenland Shelf: A numerical perspective. *Journal of Geophysical Research: Oceans*, 122, 5316–5328. <https://doi.org/10.1002/2017JC012801>
- Matishov, G., Zuyev, A., Golubev, V., Adrov, N., Slobodin, V., Levitus, S., & Smolyar, I. (1998). *Climatic atlas of the Barents Sea 1998: Temperature, salinity, oxygen (CD-ROM)*. Russia, National Oceanographic Data Center, USA: Murmansk Marine Biological Institute.
- Melling, H. (1993). The formation of a haline shelf front in wintertime in an ice-covered Arctic Sea. *Continental Shelf Research*, 13(10), 1123–1147. [https://doi.org/10.1016/0278-4343\(93\)90045-Y](https://doi.org/10.1016/0278-4343(93)90045-Y)
- Melling, H., & Moore, R. M. (1995). Modification of halocline source waters during freezing on the Beaufort Sea shelf: Evidence from oxygen isotopes and dissolved nutrients. *Continental Shelf Research*, 15(1), 89–113. [https://doi.org/10.1016/0278-4343\(94\)P1814-R](https://doi.org/10.1016/0278-4343(94)P1814-R)
- Nof, D. (1983). The translation of isolated cold eddies on a sloping bottom. *Deep Sea Research*, 41(3), 399–425. <https://doi.org/10.1357/002224083788519687>
- Nurser, A. J. G., & Bacon, S. (2014). Eddy length scales and the Rossby radius in the Arctic Ocean. *Ocean Science*, 10, 967–975. <https://doi.org/10.5194/os-10-967-2014>
- O’Dea, E., Furner, R., Wakelin, S., Siddorn, J., While, J., Sykes, P., et al. (2017). The CO5 configuration of the 7 km Atlantic Margin Model: Large-scale biases and sensitivity to forcing, physics options and vertical resolution. *Geoscientific Model Development*, 10(8), 2947–2969. <https://doi.org/10.5194/gmd-10-2947-2017>
- Oki, T., & Sud, Y. C. (1998). Design of Total Runoff Integrating Pathways (TRIP)—A global river channel network. *Earth Interactions*, 2(1), 1–37. [https://doi.org/10.1175/1087-3562\(1998\)002<0001:DOTRIP>2.3.CO;2](https://doi.org/10.1175/1087-3562(1998)002<0001:DOTRIP>2.3.CO;2)
- Perovich, D. K., Richter-Menge, J. A., Jones, K. F., & Light, B. (2008). Sunlight, water, and ice: Extreme Arctic sea ice melt during the summer of 2007. *Geophysical Research Letters*, 35, L11501. <https://doi.org/10.1029/2008GL034007>
- Pickart, R. S., Moore, G. W. K., Torres, D. J., Fratantoni, P. S., Goldsmith, R. A., & Yang, J. (2009). Upwelling on the continental slope of the Alaskan Beaufort Sea: Storms, ice, and oceanographic response. *Journal of Geophysical Research*, 114, C00A13. <https://doi.org/10.1029/2008JC005009>
- Pickart, R. S., Pratt, L. J., Whitedge, T. E., Proshutinsky, A. Y., Aagaard, K., Agnew, T. A., et al. (2010). Evolution and dynamics of the flow through Herald Canyon in the western Chukchi Sea. *Deep Sea Research Part II: Topical Studies in Oceanography*, 57, 5–26. <https://doi.org/10.1016/j.dsr2.2009.08.002>

- Pickart, R. S., Torres, D. J., & Fratantoni, P. S. (2005). The East Greenland spill jet. *Journal of Physical Oceanography*, 35, 1037–1053. <https://doi.org/10.1175/JPO2734.1>
- Pickart, R. S., Weingartner, T. J., Pratt, L. J., Zimmermann, S., & Torres, D. J. (2005). Flow of winter-transformed Pacific water into the Western Arctic. *Deep Sea Research Part II: Topical Studies in Oceanography*, 52(24–26), 3175–3198. <https://doi.org/10.1016/j.dsr2.2005.10.009>
- Platov, G. A., & Golubeva, E. N. (2019). Interaction of dense shelf waters of the Barents and Kara seas with the Eddy structures. *Physical Oceanography*, 26(6), 484–503. <https://doi.org/10.22449/1573-160X-2019-6-484-503>
- Polyakov, I. V., Pnyushkov, A. V., Alkire, M. B., Ashik, I. M., Baumann, T. M., Carmack, E. C., et al. (2017). Greater role for Atlantic inflows on sea-ice loss in the Eurasian Basin of the Arctic Ocean. *Science*, 356(6335), 285–291. <https://doi.org/10.1126/science.aai8204>
- Polyakov, I. V., Rippeth, T. P., Fer, I., Alkire, M. B., Baumann, T. M., Carmack, E. C., et al. (2020). Weakening of Cold Halocline Layer Exposes Sea Ice to Oceanic Heat in the Eastern Arctic Ocean. *Journal of Climate*, 33(18), 8107–8123. <https://doi.org/10.1175/jcli-d-19-0976.1>
- Popova, E. E., Yool, A., Aksenov, Y., & Coward, A. C. (2013). Role of advection in Arctic Ocean lower trophic dynamics: A modeling perspective. *Journal of Geophysical Research: Oceans*, 118, 1571–1586. <https://doi.org/10.1002/jgrc.20126>
- Prandle, D. (1982). The vertical structure of tidal currents. *Geophysical and Astrophysical Fluid Dynamics*, 22(1–2), 29–49. <https://doi.org/10.1080/03091928208221735>
- Proshutinsky, A., Dukhovskoy, D., Timmermans, M. L., Krishfield, R., & Bamber, J. L. (2015). Arctic circulation regimes. *Philosophical Transactions of the Royal Society A*, 373(2052), 20140160. <https://doi.org/10.1098/rsta.2014.0160>
- Proshutinsky, A. Y., & Johnson, M. A. (1997). Two circulation regimes of the wind-driven Arctic Ocean. *Journal of Geophysical Research*, 102(C6), 12,493–12,514. <https://doi.org/10.1029/97JC00738>
- Quadfasel, D., Rudels, B., & Kurz, K. (1988). Outflow of dense water from a Svalbard fjord into the Fram Strait. *Deep-Sea Research*, 35, 1143–1150. [https://doi.org/10.1016/0198-0149\(88\)90006-4](https://doi.org/10.1016/0198-0149(88)90006-4)
- Quadfasel, D., Rudels, B., & Selchow, S. (1992). The Central Bank vortex in the Barents Sea: Water mass transformation and circulation. *ICES Marine Science Symposium*, 195, 40–51.
- Rudels, B. (1986). The θ -S relations in the northern seas: Implications for the deep circulation. *Polar Research*, 4(2), 133–159. <https://doi.org/10.3402/polar.v4i2.6928>
- Shapiro, G., Luneva, M., Pickering, J., & Storkey, D. (2013). The effect of various vertical discretization schemes and horizontal diffusion parameterization on the performance of a 3-D ocean model: The Black Sea case study. *Ocean Science*, 9(2), 377–390. <https://doi.org/10.5194/os-9-377-2013>
- Shapiro, G. I., & Hill, A. E. (1997). Dynamics of dense water cascades at the shelf edge. *Journal of Physical Oceanography*, 27(11), 2381–2394. [https://doi.org/10.1175/1520-0485\(1997\)027<2381:DODWCA>2.0.CO;2](https://doi.org/10.1175/1520-0485(1997)027<2381:DODWCA>2.0.CO;2)
- Shapiro, G. I., Huthnance, J. M., & Ivanov, V. V. (2003). Dense water cascading off the continental shelf. *Journal of Geophysical Research*, 108(C12), 3390. <https://doi.org/10.1029/2002JC001610>
- Shapiro, G. I., & Zatsepin, A. G. (1997). Gravity current down a steeply inclined slope in a rotating fluid. *Annales Geophysicae*, 15, 366–374. <https://doi.org/10.1007/s00585-997-0366-x>
- Smagorinsky, J. (1963). General circulation experiments with the primitive equations. *Monthly Weather Review*, 91(3), 99–164. [https://doi.org/10.1175/1520-0493\(1963\)091%3C0099:GCEWTP%3E2.3.CO;2](https://doi.org/10.1175/1520-0493(1963)091%3C0099:GCEWTP%3E2.3.CO;2)
- Song, Y., & Haidvogel, D. (1994). A semi-implicit ocean circulation model using a generalized topography-following coordinate system. *Journal of Computational Physics*, 115(1), 228–244. <https://doi.org/10.1006/jcph.1994.1189>
- Soulsby, R. L. (1983). The bottom boundary layer of the shelf sea. In B. Johns (Ed.), *Physical oceanography of coastal and shelf seas* (pp. 189–266). New York, USA: Elsevier. [https://doi.org/10.1016/S0422-9894\(08\)70503-8](https://doi.org/10.1016/S0422-9894(08)70503-8)
- Spall, M. A., Pickart, R. S., Fratantoni, P., & Plueddemann, A. (2008). Western Arctic shelfbreak eddies: Formation and transport. *Journal of Physical Oceanography*, 38(8), 1644–1668. <https://doi.org/10.1175/2007JPO3829.1>
- Storkey, D., Blaker, A. T., Mathiot, P., Megann, A., Aksenov, Y., Blockley, E. W., et al. (2018). UK Global Ocean GO6 and GO7: A traceable hierarchy of model resolutions. *Geoscientific Model Development*, 11(8), 3187–3213. <https://doi.org/10.5194/gmd-11-3187-2018>
- Tanaka, K., & Akitomo, K. (2001). Baroclinic instability of density current along a sloping bottom and the associated transport process. *Journal of Geophysical Research*, 106(C2), 2621–2638. <https://doi.org/10.1029/2000JC000214>
- Thorpe, S. A. (1988). Benthic boundary layers on slopes. In J. C. J. Nihoul & B. M. Jamart (Eds.), *Small scale turbulence and mixing in the ocean, Elsevier Oceanography Series* (Vol. 46, pp. 425–433).
- Timmermans, M. L., Proshutinsky, A., Krishfield, R. A., Perovich, D. K., Richter-Menge, J. A., Stanton, T. P., & Toole, J. M. (2011). Surface freshening in the Arctic Ocean's Eurasian Basin: An apparent consequence of recent change in the wind-driven circulation. *Journal of Geophysical Research*, 116, C00D03. <https://doi.org/10.1029/2011JC006975>
- Timmermans, M. L., Toole, J., & Krishfield, R. (2018). Warming of the interior Arctic Ocean linked to sea ice losses at the basin margins. *Science Advances*, 4(8), 6773. <https://doi.org/10.1126/sciadv.aat6773>
- Van Sebille, E., Griffies, S. M., Abernathey, R., Adams, T. P., Berloff, P., Biastoch, A., et al. (2018). Lagrangian ocean analysis: Fundamentals and practices. *Ocean Modelling*, 121, 49–75. <https://doi.org/10.1016/j.ocemod.2017.11.008>
- Weatherley, G. L., & Martin, P. G. (1978). On the structure and dynamics of the oceanic boundary layer. *Journal of Physical Oceanography*, 8, 557–570. [https://doi.org/10.1175/1520-0485\(1978\)008<0557:otsado>2.0.co;2](https://doi.org/10.1175/1520-0485(1978)008<0557:otsado>2.0.co;2)
- Weingartner, T., Aagaard, K., Woodgate, R., Danielson, S., Sasaki, Y., & Cavalieri, D. (2005). Circulation on the north central Chukchi Sea shelf. *Deep Sea Research Part II: Topical Studies in Oceanography*, 52(24–26), 3150–3174. <https://doi.org/10.1016/j.dsr2.2005.10.015>
- Weingartner, T. J., Cavalieri, D. J., Aagaard, K., & Sasaki, Y. (1998). Circulation, dense water formation, and outflow on the northeast Chukchi shelf. *Journal of Geophysical Research*, 103(C4), 7647–7661. <https://doi.org/10.1029/98JC00374>
- Wimbush, M., & Munk, W. (1970). The benthic boundary layer. In A. E. Maxwell (Ed.), *The Sea* (Vol. 4(1), pp. 731–758). New York: Wiley-Interscience.
- Winsor, P., & Björk, G. (2000). Polynya activity in the Arctic Ocean from 1958 to 1997. *Journal of Geophysical Research*, 105(C4), 8789–8803. <https://doi.org/10.1029/1999JC900305>
- Winton, M., Hallberg, R., & Gnanadesikan, A. (1998). Simulation of density-driven frictional downslope flow in z-coordinate ocean models. *Journal of Physical Oceanography*, 28(11), 2163–2174. [https://doi.org/10.1175/1520-0485\(1998\)028<2163:SODDFD>2.0.CO;2](https://doi.org/10.1175/1520-0485(1998)028<2163:SODDFD>2.0.CO;2)
- Wobus, F., Shapiro, G. I., Huthnance, J. M., & Maqueda, M. A. (2013). The piercing of the Atlantic layer by an Arctic shelf water cascade in an idealised study inspired by the Storfjorden overflow in Svalbard. *Ocean Modelling*, 71, 54–65. <https://doi.org/10.1016/j.ocemod.2013.03.003>

- Wobus, F., Shapiro, G. I., Huthnance, J. M., Maqueda, M. A. M., & Aksenov, Y. (2013). Tidally induced lateral dispersion of the Storfjorden overflow plume. *Ocean Science*, 9(5), 885–899. <https://doi.org/10.5194/os-9-885-2013>
- Wobus, F., Shapiro, G. I., Maqueda, M. A., & Huthnance, J. M. (2011). Numerical simulations of dense water cascading on a steep slope. *Journal of Marine Research*, 69(2–3), 391–415. <https://doi.org/10.1357/002224011798765268>
- Woodgate, R. A., Aagaard, K., & Weingartner, T. J. (2005). A year in the physical oceanography of the Chukchi Sea: Moored measurements from autumn 1990–1991. *Deep Sea Research Part II: Topical Studies in Oceanography*, 52(24–26), 3116–3149. <https://doi.org/10.1016/j.dsr2.2005.10.016>
- Zhong, W., Steele, M., Zhang, J., & Cole, S. T. (2018). Circulation of Pacific winter water in the Western Arctic Ocean. *Journal of Geophysical Research: Oceans*, 124, 863–881. <https://doi.org/10.1029/2018JC014604>